https://doi.org/10.5194/egusphere-2026-5136
Preprint. Discussion started: 31 August 2026

Stability and basal thermal conditions of East Antarctic divide regions during the last glacial cycle

Olivia Raspoet[1], Violaine Coulon[1], and Frank Pattyn[1]

[1]Laboratoire de Glaciologie, Université libre de Bruxelles

Correspondence: Olivia Raspoet (olivia.raspoet@ulb.be)

Abstract. Ice domes and divides of the East Antarctic Ice Sheet (EAIS) are primary targets for deep ice core drilling because of their presumed stability and cold basal conditions. These characteristics are essential for preserving undisturbed and continuous stratigraphy, which is critical for interpreting climate proxies from ice core records. Here, we conduct an ensemble of transient thermomechanical simulations of the Antarctic ice sheet over the last glacial cycle to evaluate the stability of six regions identified as potential candidates for deep ice core drilling. The evolution of the basal thermal regime and its response to climate forcing are also assessed. Results indicate that domes and divides of the EAIS remained relatively stable throughout the last glacial cycle, with displacements occurring primarily within 20 to 40 km of their initial positions and elevation changes ranging from 50 to 150 m between glacial and interglacial periods. Dome migration is primarily driven by changes in local accumulation patterns and large-scale grounding-line migration. Basal temperatures and melt rates exhibit a lagged response to climate forcing of approximately 17 to 35 ka, suggesting that present-day basal thermal conditions still reflect the cooler climate of the Last Glacial Maximum. Finally, we find favourable thermodynamic conditions for the preservation of ancient ice at the base in all but one of the studied regions, and use this information to identify and map potential drilling sites across Antarctica. However, estimates of the thermal state are highly sensitive to geothermal heat flow and even minor inaccuracies in modelled ice thickness, indicating that local constraints are required to better decipher conditions at the ice-bedrock interface.

1 Introduction

Ice cores serve as unique continuous archives of past climatic conditions, enabling the reconstruction of historical temperatures and atmospheric composition (Bouchet et al., 2023). In Antarctica, several deep ice cores provide extensive climate records, including the EPICA Dome C (800 ka; Jouzel et al., 2007), Dome Fuji (720 ka; Kawamura et al., 2017; Uemura et al., 2018), and Vostok (420 ka; Petit et al., 1999) ice cores. Within the framework of the Beyond EPICA project, a new ice core was recently drilled at Little Dome C (LDC; BELDC; e.g., Lilien et al., 2021; Chung et al., 2023; Westhoff et al., 2026), with the aim of recovering a climate record spanning at least the last 1.2 million years. This effort is expected to advance our understanding of the climate system and disentangle the mechanisms associated with the mid-Pleistocene transition (MPT; Lisiecki and Raymo, 2005; Snyder, 2016), during which the periodicity of glacial-interglacial cycles changed from 40 to 100 ka. Additional candidate sites, which might have preserved old ice in continuous ice records, are under investigation (e.g., Van Liefferinge et al., 2018; Sutter et al., 2019), notably in the regions surrounding Dome Fuji (e.g., Karlsson et al., 2018;

https://doi.org/10.5194/egusphere-2026-5136
Preprint. Discussion started: 31 August 2026

Wang et al., 2023b; Obase et al., 2023), Dome Argus (e.g., Xiao et al., 2008; Zhao et al., 2018; Sanderson et al., 2024; Li et al., 2026), Ridge B (e.g., Ekaykin et al., 2021, 2023; Lang et al., 2025), and South Pole (e.g., Beem et al., 2021).

Ice domes and divides of the East Antarctic Ice Sheet (EAIS) are primary targets for deep ice-core drilling because of their location in slow-flowing regions that minimise horizontal ice advection, which is favourable for the preservation of continuous and undisturbed englacial stratigraphy suitable for long-term climate reconstructions (e.g., Gillet-Chaulet and Hindmarsh, 2011; Fischer et al., 2013; Parrenin et al., 2017; Winter et al., 2019). One of the major challenges in interpreting ice cores lies in establishing an accurate chronology (i.e., the relationship between the age of ice and its depth) and determining the spatial origin and past trajectories of ice particles (Parrenin et al., 2004). These are crucial for dating past climate events and interpreting the climatic and environmental signals preserved in the ice (Bouchet et al., 2023). This age-depth relationship is typically determined using internal ice layers, radar stratigraphy, and ice-flow models. However, these ice-flow models often assume a stable dome position over time (e.g., Leysinger Vieli et al., 2011; Bazin et al., 2013; Parrenin et al., 2017; Bouchet et al., 2023), although the assumption of dome stationarity is challenged by both modelling and observational studies revealing dome displacements over glacial (e.g., Sutter et al., 2019; van Aalderen et al., 2026; Wirths et al., 2026) and decadal to centennial timescales (e.g., Urbini et al., 2008; Vittuari et al., 2025).

The position and stability of ice domes and divides can be influenced by variations in surface accumulation patterns (e.g., Nereson et al., 1998; Urbini et al., 2008), large-scale changes in ice-sheet geometry (including ice thickness variations, glacial isostatic adjustment, and grounding line retreat), subsequent reorganisation in ice-flow and boundary fluxes (e.g., Gillet-Chaulet and Hindmarsh, 2011), and basal conditions (e.g., Sutter et al., 2019). These temporal changes in dome position can complicate ice core analysis by disrupting internal layering, displacing previously preserved ancient ice, and altering the origin of ice particles. To address these complexities, studies have employed flowband models to account for both vertical and horizontal flow variations (e.g., Parrenin et al., 2004; Passalacqua et al., 2016; Koutnik et al., 2016; Chung et al., 2025). Radar-derived internal stratigraphy has also been used to infer the history of dome stability and ice geometry (e.g., Nereson et al., 1998; Nereson and Waddington, 2002; Price et al., 2007; Martín et al., 2009; Hills et al., 2025). Despite these efforts, past trajectories of EAIS domes remain highly uncertain, especially over glacial-interglacial timescales.

In addition, basal thermal conditions are critical for the long-term preservation of old ice at the bottom of the ice column. The thermal state of the ice-bed interface controls basal melting, which can erode ancient layers and compromise the continuity of climate records derived from ice cores (Fischer et al., 2013; Van Liefferinge and Pattyn, 2013). This is why old-ice exploration efforts preferentially target cold-based regions with low geothermal heat flow (e.g., Fischer et al., 2013; Van Liefferinge and Pattyn, 2013; Parrenin et al., 2017; Passalacqua et al., 2017). Moreover, basal melting and freeze-on can affect ice-core interpretations by disrupting basal ice stratigraphy and the age-depth relationship (e.g., Parrenin et al., 2004; Leysinger Vieli et al., 2018).

Basal temperatures and melt rates result from a complex interplay between several processes, including geothermal heat flow (GHF), frictional heating, ice thickness and climate evolution (Raspoet and Pattyn, 2025a), leading to uncertain and spatially heterogeneous basal thermal conditions beneath the East Antarctic Plateau (Dawson et al., 2022; Raspoet and Pattyn, 2025a; Seiner et al., 2025). Although ice-sheet models have performed transient glacial-interglacial thermomechanical simulations

https://doi.org/10.5194/egusphere-2026-5136
Preprint. Discussion started: 31 August 2026

(e.g., Ritz, 1987; Huybrechts, 1992; Ritz et al., 2001; Sutter et al., 2019; Albrecht et al., 2020a; Berends et al., 2021; Lecavalier and Tarasov, 2025), the evolution of basal temperatures and melt rates is often overlooked or rely on simplified thermodynamic models (e.g., Passalacqua et al., 2017; Van Liefferinge et al., 2018; Obase et al., 2023), and recent studies on the Antarctic basal thermal state tend to assume a thermal steady state (i.e., equilibrium with respect to present-day climatic conditions; e.g., Dawson et al., 2022; Park et al., 2024; Raspoet and Pattyn, 2025a), so that Antarctic subglacial conditions and their evolution over glacial-interglacial timescales remain poorly constrained. The latter merits special attention because present-day thermal conditions may not be representative of all previous glacial-interglacial periods, and current cold-based regions may reflect cooling from the last glacial period (Passalacqua et al., 2017).

Numerical ice-sheet models can determine changes in ice-flow patterns, ice-sheet elevations, and basal thermal conditions over the time scales of ice-core records (e.g., Sutter et al., 2019; Wirths et al., 2025). Here, we investigate the stability of East Antarctic divide regions and the evolution of their basal conditions using an ensemble of transient thermomechanical ice-sheet simulations spanning the last glacial-interglacial cycle. Although longer periods are not considered for computational reasons, the most recent glacial-interglacial cycle serves as a useful reference for the last 800 ka, as it captures much of the temperature variability observed during this interval (Jouzel et al., 2007). This ensemble of palaeo ice-sheet simulations allows us to assess changes in the flow pattern of the divide area that influence key potential drilling sites and evaluate changes in ice elevation. The latter is important for correcting isotope data for local temperature differences caused by past elevation changes (Buizert et al., 2021). Finally, we analyse the evolution of basal thermal conditions over the same period as a function of different GHF estimates, and use this information to identify potential suitable drilling sites for the research of the oldest-ice across Antarctica. This work aims to contribute to ongoing efforts to identify potential oldest-ice candidates, refine the interpretation of ice-core records, and inform strategies for future drilling campaigns.

2 Methods

2.1 Ice sheet model

The evolution of the Antarctic Ice Sheet (AIS) is simulated with the Kori-ULB ice sheet model (v0.92; https://github.com/FrankPat/Kori-ULB; Pattyn, 2017). Kori-ULB is a hybrid ice-sheet/ice-shelf model that combines shallow ice (SIA) and shallow shelf (SSA) approximations to simulate ice flow over grounded and floating ice (Bueler and Brown, 2009; Winkelmann et al., 2011). A flux condition (Schoof, 2007) is prescribed at the grounding line to capture grounding-line migration given the coarse resolution of our model simulations (25 km; Schoof, 2007; Pollard and DeConto, 2012a, 2020). Basal melting under floating ice shelves is calculated with the Potsdam Ice Shelf Cavity Model (PICO; Reese et al., 2018) and calving at the ice front is determined by combining penetration depths of surface and basal crevasses relative to total ice thickness (Pollard et al., 2015; DeConto and Pollard, 2016). The model includes two thermodynamic solvers based on cold-ice or enthalpy methods (Raspoet and Pattyn, 2025a) and full thermomechanical coupling (Ritz, 1987, 1992), where shape functions are used to represent the vertical profiles of horizontal and vertical velocities, considering increased strain rates due to warmer and more deformable ice near the base (Lliboutry, 1979; Hindmarsh, 1999; Hindmarsh et al., 2009). Basal sliding follows a power law with a power-law exponent

https://doi.org/10.5194/egusphere-2026-5136
Preprint. Discussion started: 31 August 2026

$m = 3$ (Weertman, 1957; Budd et al., 1979; Budd and Jenssen, 1987). Glacial isostatic adjustment (GIA) is represented by an Elastic Lithosphere-Relaxing Asthenosphere (ELRA) model (Coulon et al., 2021) with spatially variable flexural rigidity (Chen et al., 2018) and relaxation times (van Calcar et al., 2026). As widely assumed in palaeo-ice-sheet modelling studies (e.g., Sutter et al., 2019; Albrecht et al., 2020a; Chandler et al., 2025), we neglect self-consistent gravitational effects from the local sea-level variations and the Earth's rotational state.

The model is initialised with a transient inverse simulation under constant present-day climatic conditions (defined as the mean climatic conditions for the 1995-2014 period), during which basal sliding coefficients under the grounded ice sheet and sub-shelf melt rates beneath floating ice shelves are iteratively adjusted to minimise the difference between modelled and observed ice thickness (Pollard and DeConto, 2012b; Bernales et al., 2017), while the calving front remains fixed at its present-day observed position. This is followed by a short relaxation run under constant atmospheric and oceanic conditions to limit the impact of transitioning from optimised sub-shelf melt rates to those calculated with the PICO model (Coulon et al., 2025). Subsequently, a long-term diagnostic (i.e., fixed ice-sheet geometry) thermal memory run is conducted using reconstructions of surface temperature anomalies over the past 800 ka (Jouzel et al., 2007) to capture transient thermal effects associated with past climate changes. The resulting ice sheet state at 130 ka BP (BP: before present) is used as an initial state for the palaeo simulations, during which the model is forced over the last glacial cycle (starting at the last interglacial) with full model physics, as described above (Figure S1). This approach yields an initial state which captures the imprint of the past climate history in the englacial temperature field while maintaining an ice sheet geometry close to the observed one (Figures S2–S4), assuming that the ice-sheet geometry at 130 ka BP was close to the present-day configuration.

Due to the computational cost associated with high-resolution simulations, a coarse spatial resolution of 25 km was employed, consistent with other modelling studies of the AIS on glacial-interglacial timescales, e.g., 16 km in Albrecht et al. (2020a) and Chandler et al. (2025); 16 and 20 km in Wirths et al. (2026); 40 km in Quiquet et al. (2018), van Calcar et al. (2023), and Lecavalier and Tarasov (2025). Additional experiments spanning shorter time scales (10 ka) were also performed at 16 km under idealised LIG and LGM conditions to assess the sensitivity of our model simulations to the spatial resolution. Results indicate similar behaviour in terms of grounded ice sheet extents and volumes, dome migration patterns, and basal conditions across the dome regions for both resolutions (Figures S12–S18). Although further divergence may occur at higher resolutions, these remain computationally prohibitive for multi-millennial Antarctic-wide simulations.

2.2 Palaeoclimate forcings

Time-dependent atmospheric and oceanic forcings are reconstructed using either an ice core forcing or a climate index approach (Figure S1 panel b). Both methods allow for satisfactorily capturing variations in surface temperatures and surface accumulation rates evidenced by ice core reconstructions (e.g., Buizert et al., 2021; Figures S5–S6).

The ice core forcing consists of applying a spatially uniform change in the background surface temperature using ice core temperature reconstructions. Here, we employ surface temperature anomalies derived from the EPICA Dome C record (Jouzel et al., 2007). At each time step, the near-surface temperature is further corrected for ice-sheet elevation changes according to

https://doi.org/10.5194/egusphere-2026-5136
Preprint. Discussion started: 31 August 2026

the environmental lapse rate (Huybrechts, 1998; Pollard and DeConto, 2012a):

$$T_s(t) = T_s^0 + \Delta T_s(t) + \gamma(h_s - h_s^0) \tag{1}$$

where $T_s(t)$ is the transient surface temperature, T_s^0 is the initial surface temperature, h_s is the surface elevation, h_s^0 is the initial surface elevation, $\gamma = -0.008$ °C m^{-1} is the environmental lapse rate, and ΔT_s is the surface temperature anomaly. The precipitation field P is modified as a function of surface temperature changes, following a relationship derived from an analysis of CMIP5 models (Frieler et al., 2015; Golledge et al., 2015):

$$P(t) = P^0 \times (1 + F_P(\gamma(h_s - h_s^0) + \Delta T_s(t))) \tag{2}$$

where $P(t)$ and P^0 represent transient and initial precipitation fields, respectively, and $F_P = 0.053$ is a sensitivity factor for precipitation change with temperature (Frieler et al., 2015). This parametrisation leads to lower accumulation rates with decreased surface temperatures. The surface melt and runoff are calculated with a positive degree-day (PDD) model that uses the near-surface air temperature and the precipitation rate as inputs, along with parameters listed in Table A1 (Reeh, 1991; Calov and Greve, 2005; Coulon et al., 2024). Finally, the ocean temperature is obtained by applying a temperature offset to the initial ocean thermal conditions:

$$T_o(t) = T_o^0 + (F_M \Delta T_s) \tag{3}$$

where $T_o(t)$ and T_o^0 correspond to transient and initial ocean temperature fields, respectively, and $F_M = 0.25$ is an ocean melt factor that represents the ratio between oceanic and atmospheric temperature changes (Maris et al., 2014; Golledge et al., 2015), which has been shown to reproduce trends in ocean temperatures (Golledge et al., 2015).

Alternatively, the climate index approach allows reconstruction of transient and spatially varying climate forcings using time slices from Earth System Models (ESMs) or Global Climate Models (GCMs). Following the methodology of Sutter et al. (2016) and Sutter et al. (2019), we derive a climate index from the EPICA Dome C deuterium record (Jouzel et al., 2007). This climate index enables temporal interpolation of climate time slices of the Last Interglacial (LIG; 130 ka BP) and Last Glacial Maximum (LGM; 21 ka BP), which are obtained from the *lig127k* and *lgm* experiments of the fourth phase of the Paleoclimate Modelling Intercomparison Project (PMIP4). We employ time slices from MIROC-ES2L (Ohgaito et al., 2019; O'ishi et al., 2019; Hajima et al., 2019; Ohgaito et al., 2021), as this ESM is among the few in PMIP4 that provide data for both the LIG and LGM periods. Because climate snapshots are interpolated every century, the deuterium record used to derive the climate index is smoothed to reflect the average trend of each century. For each climate time slice, atmospheric and oceanic anomalies relative to the 1995-2014 period are derived from ESM projections and combined with present-day atmospheric and oceanic conditions (Coulon et al., 2024, 2025) using a linear scaling factor (Sutter et al., 2019):

$$T_s(t) = T_s^0 + \omega^{\mathrm{LIG}}(t)\Delta T_s^{\mathrm{LIG}} + \omega^{\mathrm{LGM}}(t)\Delta T_s^{\mathrm{LGM}} \tag{4}$$

where $\Delta T_s^{\mathrm{LIG}}$ and $\Delta T_s^{\mathrm{LGM}}$ are surface temperature anomalies for LIG and LGM periods, $\omega^{\mathrm{LIG}} = (\max(\mathrm{CI}, \mathrm{CI}^{\mathrm{PD}}) - \mathrm{CI}^{\mathrm{PD}})/(1 - \mathrm{CI}^{\mathrm{PD}})$ and $\omega^{\mathrm{LGM}} = 1 - \min(\mathrm{CI}, \mathrm{CI}^{\mathrm{PD}})/\mathrm{CI}^{\mathrm{PD}}$ are the scaling factors for LIG and LGM, and $\mathrm{CI}^{\mathrm{PD}}$ refers to the present-day

https://doi.org/10.5194/egusphere-2026-5136
Preprint. Discussion started: 31 August 2026

climate index (Sutter et al., 2019). The climate index is normalized so that $\mathrm{CI}^{\mathrm{LIG}} = 1$ and $\mathrm{CI}^{\mathrm{LGM}} = 0$. The same logic is applied to ocean temperature and salinity fields. Missing values on the continental shelf and in currently ice-covered regions are extrapolated, and the GCM-derived ocean conditions are vertically interpolated at the depth of the continental shelf following Kreuzer et al. (2021). We employ precipitation ratios instead of precipitation anomalies to avoid negative absolute precipitation (Goosse et al., 2010). Surface melt and runoff are simulated with the PDD model (Reeh, 1991; Calov and Greve, 2005; Coulon et al., 2024). Near-surface air temperatures are adjusted for variations in ice-sheet surface elevation according to the atmospheric lapse rate, which accounts for the surface melt-elevation feedback.

2.3 Ensemble design and scoring

We perform an ensemble of 160 simulations using full-factorial sampling (i.e., one simulation is conducted for every possible combination of factors; Pollard et al., 2016; Albrecht et al., 2020b) to explore uncertainties in the climate-forcing approach, boundary conditions, bedrock deformation, and ice thermodynamics. We do not perform a wide parameter-space exploration for robust uncertainty analysis. Instead, parameters were selected through preliminary manual tuning based on model performance. The factors of uncertainty considered in this study are summarised in Table 1. A non-exhaustive list of model parameters is also provided in Table A1.

Initial surface temperatures and accumulation rates are prescribed from the outputs of the Modèle Atmosphérique Régional (MAR v3.11; Kittel et al., 2021) and the polar Regional Atmospheric Climate Model (RACMO 2.3p2; van Wessem et al., 2018) over the 1995-2014 period, while the climate forcing is derived using the ice core forcing or climate index approach (see above). We prescribe a sea-level offset based on the global sea-level reconstructions of Bintanja and Van de Wal (2008) and Spratt and Lisiecki (2016), which influences the grounding line position through floatation. The Earth's rheological properties used to define relaxation times in the ELRA model are taken from van Calcar et al. (2026), which includes stronger (GIAS) or weaker (GIAW) Earth structures. We consider five GHF datasets to assess the evolution of basal conditions (Martos et al., 2017; Shen et al., 2020; Stål et al., 2021; Lösing and Ebbing, 2021; Haeger et al., 2022), in combination with cold-ice and enthalpy solvers for ice thermodynamics (Raspoet and Pattyn, 2025a). The GHF datasets were chosen based on their performance in an ensemble of thermal modelling of the AIS (Raspoet and Pattyn, 2025a) and recommendations of the geophysical community (Lösing et al., 2026). Finally, all simulations use present-day ocean temperature and salinity fields from Schmidtko et al. (2014). The initial bed topography, surface elevation, and ice thickness are taken from MEaSUREs BedMachine v3 (Morlighem et al., 2020; Morlighem, 2022).

We score our ensemble of simulations based on their ability to reproduce present-day and past ice-sheet configurations, closely following the approach described in Pollard et al. (2016) and Albrecht et al. (2020b). This approach enables the computation of an aggregate score for each ensemble member, quantifying the misfit between the model results and a selected set of modern observational and geological constraints. For that purpose, we use the MEaSUREs present-day ice thickness, grounding line extent (BedMachine v3; Morlighem et al., 2020; Morlighem, 2022), surface velocities (Phase-Based Antarctica Ice Velocity Map v1; Mouginot et al., 2019a, b) as well as the Reconstruction of Antarctic Ice Sheet Deglaciation (RAISED consortium; Bentley et al., 2014) and the Antarctic ice sheet palaeo constraint database (AntICE2; Lecavalier et al., 2023).

https://doi.org/10.5194/egusphere-2026-5136
Preprint. Discussion started: 31 August 2026

Table 1. Factors of uncertainty considered in this study.

Factors of uncertainty		References
Atmospheric present-day climatology (CLIM0)	MAR v3.11	Kittel et al. (2021)
	RACMO 2.3p2	van Wessem et al. (2018)
Climate forcing (FORCING)	Ice core forcing	Huybrechts (1998); Pollard and DeConto (2012a); Golledge et al. (2015)
	Climate index	Sutter et al. (2019)
Sea level forcing (SLR)		Bintanja and Van de Wal (2008)
		Spratt and Lisiecki (2016)
Glacial Isostatic Adjustment (GIA)*	GIAS	van Calcar et al. (2026)
	GIAW	van Calcar et al. (2026)
Ice thermodynamics (THERMO)	Cold-ice	Raspoet and Pattyn (2025a)
	Enthalpy	Raspoet and Pattyn (2025a)
Geothermal heat flow (GHF)		Shen et al. (2020)
		Martos et al. (2017)
		Stål et al. (2021)
		Lösing and Ebbing (2021)
		Haeger et al. (2022)

*Relaxation times in the GIA model.

The misfit score is derived with a general observational error model that assumes Gaussian-distributed errors and accounts for uncertainties in the interpretation of the observations (Albrecht et al., 2020b). The aggregated score is then used to calculate a weight for each ensemble member. The procedure to calculate the misfit for each data type and to aggregate scores is detailed in Appendix B. Qualitative assessment of the modelled results with respect to the observational constraints is also presented in the supplementary material (Figures S3, S7–S11).

2.4 Tracking of dome migration

We focus our analysis on the migration of six domes and ice divide regions of East Antarctica that have been reported as potential candidates for deep ice core drilling: Dome F (e.g., Karlsson et al., 2018; Wang et al., 2023b; Obase et al., 2023), Dome C (e.g., Parrenin et al., 2007, 2017; Passalacqua et al., 2017; Lilien et al., 2021; Chung et al., 2023), Dome A (e.g., Xiao et al., 2008; Sun et al., 2014; Sanderson et al., 2024; Zhao et al., 2018; Wang et al., 2023a; Li et al., 2026), Ridge B (e.g., Ekaykin et al., 2021; Lang et al., 2025), Titan Dome (e.g., Beem et al., 2021) and Hercules Dome (e.g., Jacobel et al., 2005; Fudge et al., 2023; Hills et al., 2025). The first four regions are considered likely to host favourable conditions for preservation

https://doi.org/10.5194/egusphere-2026-5136
Preprint. Discussion started: 31 August 2026

of ancient ice at the base in the regions surrounding the domes (e.g., frozen conditions because of lower ice thickness than at the dome; Van Liefferinge et al., 2018; Sutter et al., 2019), whereas the last two are identified as promising sites for obtaining high-resolution ice cores that resolve the last glacial-interglacial cycle (e.g., Beem et al., 2021; Hills et al., 2025). However, the analysis presented in this study can be easily extended to other locations as our ensemble of simulations covers the whole AIS. The positions of the selected domes are tracked every 1000 years and are determined by locating the grid point that exhibits the highest surface elevation in a 2D spline within a defined domain extending around the current dome position. The size of the domain was determined based on current topographic features, so that the current dome position is adequately captured by the algorithm. We therefore track the movement of the topographic dome, contrary to other approaches that use ice velocity gradients (e.g., van Aalderen et al., 2026; Wirths et al., 2026). Nevertheless, the position of the topographic domes generally coincides closely with the ice flow divergence pattern observed across the divide (Figure S19–S23).

3 Results

3.1 Evolution of the AIS during the last glacial cycle

Figure 1a shows the results of the ensemble mean of Antarctic simulations over the last glacial cycle, weighted according to the ability of the ensemble members to reproduce geological and glaciological observational constraints (Appendix B). The results indicate progressive ice sheet growth from the LIG to the LGM (25-15 ka BP), with most simulations showing expansion toward the continental shelf, followed by widespread retreat during deglaciation beginning around 12 ka BP, consistent with previous model studies (e.g., Albrecht et al., 2020a; Lecavalier and Tarasov, 2025). The ensemble demonstrates close agreement with the reconstruction of the Antarctic ice sheet deglaciation (RAISED consortium; Bentley et al., 2014), except at 10 ka BP, when most simulations show faster deglaciation and earlier retreat in the Ross Sea sector compared to the reconstruction (Figure S8). The ensemble weighted mean results also converge with AntICE2 palaeo-reconstructions (Figure S9; Lecavalier et al., 2023), which mostly cover the deglaciation and Holocene periods, as well as with modern observations of the present-day (PD) ice-sheet configuration at 0 ka BP (Figure S7; Morlighem et al., 2020). The ensemble does not exhibit a substantial retreat during the LIG (130–115 ka BP), either in the East Antarctic Ice Sheet (EAIS) subglacial basins or the West Antarctic Ice Sheet (WAIS), in contrast to evidence highlighted in Bentley and Wolff (2026). Approximately 30% of ensemble members display grounding line retreat in the Amundsen Sea sector, and 50% exhibit a slight retreat in the Siple Coast region (Figure S19). However, a substantial retreat occurs in the WAIS in sensitivity experiments when the ice sheet is forced under sustained LIG conditions for 10 ka (Figure S12, panel b).

Figure 1b presents the evolution of the modelled grounded ice sheet area and volume, along with the factors contributing to the ensemble spread, as determined through a variance-based sensitivity analysis (Appendix C). The climate forcing approach (FORCING) and sea level forcing (SLR) explain most of the variability in the grounded ice sheet area and volume, although their relative contributions vary in time. Simulations using the climate index approach lead to larger modelled grounded ice volumes and areas, along with a slightly delayed deglaciation (Figure S24). This is associated with weaker amplitude changes in the atmospheric forcing, which produce higher surface accumulation rates during the glacial period compared to the ice

https://doi.org/10.5194/egusphere-2026-5136
Preprint. Discussion started: 31 August 2026

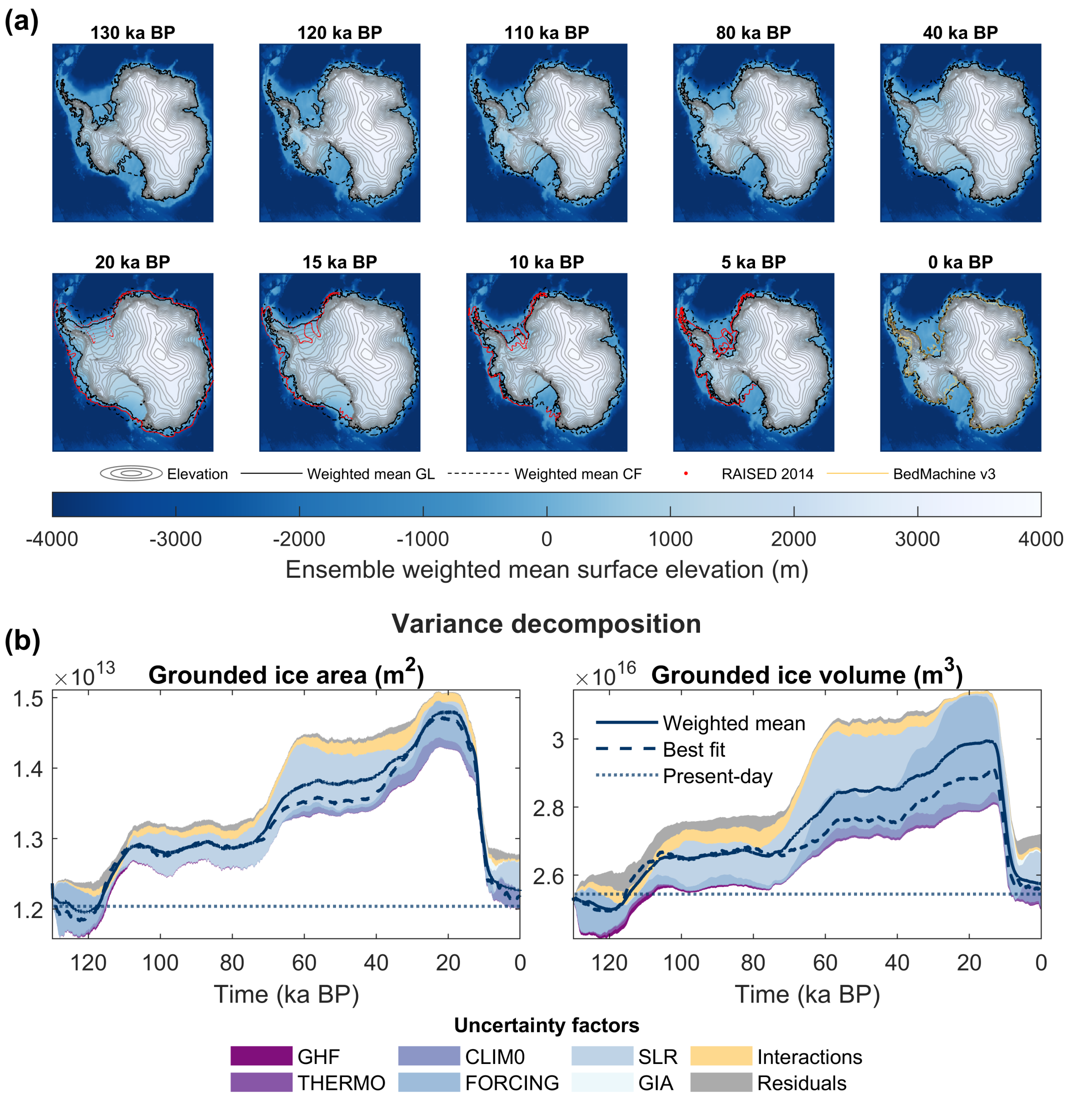

Figure 1. Evolution of the Antarctic ice sheet during the last glacial cycle. (a) Ensemble weighted mean surface elevations and grounding line positions during the last glacial cycle. The red and yellow contours indicate the Reconstruction of the Antarctic Ice Sheet Deglaciation (RAISED consortium; Bentley et al., 2014) and BedMachine v3 (Morlighem et al., 2020; Morlighem, 2022) grounding line positions, respectively. (b) Evolution of the grounded ice-sheet area and volume during the last glacial cycle. The plain and dashed lines highlight the ensemble-weighted mean and the best-fit simulation, respectively. The dotted lines represent the present-day values (BedMachine v3; Morlighem et al., 2020; Morlighem, 2022). The colours highlight the contributions of the different factors of uncertainty considered in this study (Table 1), determined through a variance decomposition analysis (ANOVA; Appendix C), within the ensemble uncertainty range. GL: grounding line. CF: calving front. BP: before present.

https://doi.org/10.5194/egusphere-2026-5136
Preprint. Discussion started: 31 August 2026

core forcing approach (Figures S5–S6). For similar reasons, initial climatic conditions from MAR also yield simulations with larger ice sheets than those from RACMO (Figure S25). Sea level forcing based on Bintanja and Van de Wal (2008) produces higher grounded ice areas and volumes than Spratt and Lisiecki (2016). No significant differences are observed between simulations using GIAS and GIAW configurations, likely due to the similarity of the two relaxation-time maps in West Antarctica, where most changes in ice-sheet geometry occur (Figure S10 a–b). However, GIA remains a critical factor in simulating the evolution of the AIS during the last glacial cycle, particularly during the deglaciation. Simulations that do not consider GIA or use alternative relaxation times do not reproduce the deglaciation and present-day ice sheet configuration as accurately (Figure S26). Finally, the ensemble demonstrates limited sensitivity to the choice of the ice thermodynamical model and GHF when simulating large-scale ice sheet behaviour (Figure S25).

3.2 Dome migration and surface elevation changes

Figure 2 illustrates the location of the domes and their evolution throughout the last glacial cycle. Five of the six selected regions demonstrate favourable conditions for the preservation of old ice at the base (Figure 2), with likely cold basal conditions (in this study and in Raspoet and Pattyn, 2025a), slow flowing ice (v < 2.5 m a^{-1}), and substantial ice thickness (H > 2000 m) (Fischer et al., 2013; Van Liefferinge and Pattyn, 2013). Dome migration is further quantified by computing the distance and orientation relative to the final position at 0 ka BP (Figure 3). On average, the domes remain relatively stable over time, staying within approximately 30 km of their original positions. Given the initialisation procedure, the modelled initial position of each dome starts closely from the currently observed location (black squares in Figure 2). As a consequence, the final positions of all domes do not always converge exactly with the current observations. However, the trajectories still provide useful information on dome migration patterns during the last glacial cycle (coloured circles in Figure 2).

Despite their overall stability, the domes exhibit distinct migration patterns (Figures 3; S27a). Dome F remains relatively stable, with migration primarily toward the southeast within approximately 20 [0–40] km (5–95% interval) of its original position. Dome A migrates mainly to the east, within approximately 45 [0–100] km of its initial position. Dome C exhibits the most complex migration, initially moving south during the LIG, then north at the onset of glaciation, followed by alternating southeast and northeast movements, reaching its maximum displacement during deglaciation before returning toward its preglacial position. This migration occurs within approximately 40 [0–145] km of the original position. Ridge B shifts slightly northward, remaining within approximately 20 [0–40] km of its initial position. Titan Dome and Hercules Dome migrate to the northeast within approximately 40 [0–80] km and 15 [0–20] km, respectively. Small circular dome displacements, associated with cooling and warming phases during the glacial period, are a common pattern across all domes (Figure S27a). Subsequently, Titan Dome and Hercules Dome progressively return to their initial positions during the Holocene, whereas the others move toward their pre-LGM positions. This reflects a lagged response to climate forcing resulting from slower response times for the domes with larger ice thicknesses.

The drivers for the ensemble spread vary in time and by location (Figure S28). For instance, GHF has a non-negligible influence on the migration of Dome F and Dome A, especially during the LIG period and early stages of glaciation, but has limited impact on Dome C, Ridge B, and Titan Dome migrations and thickness changes. Ridge B is more influenced by

https://doi.org/10.5194/egusphere-2026-5136
Preprint. Discussion started: 31 August 2026

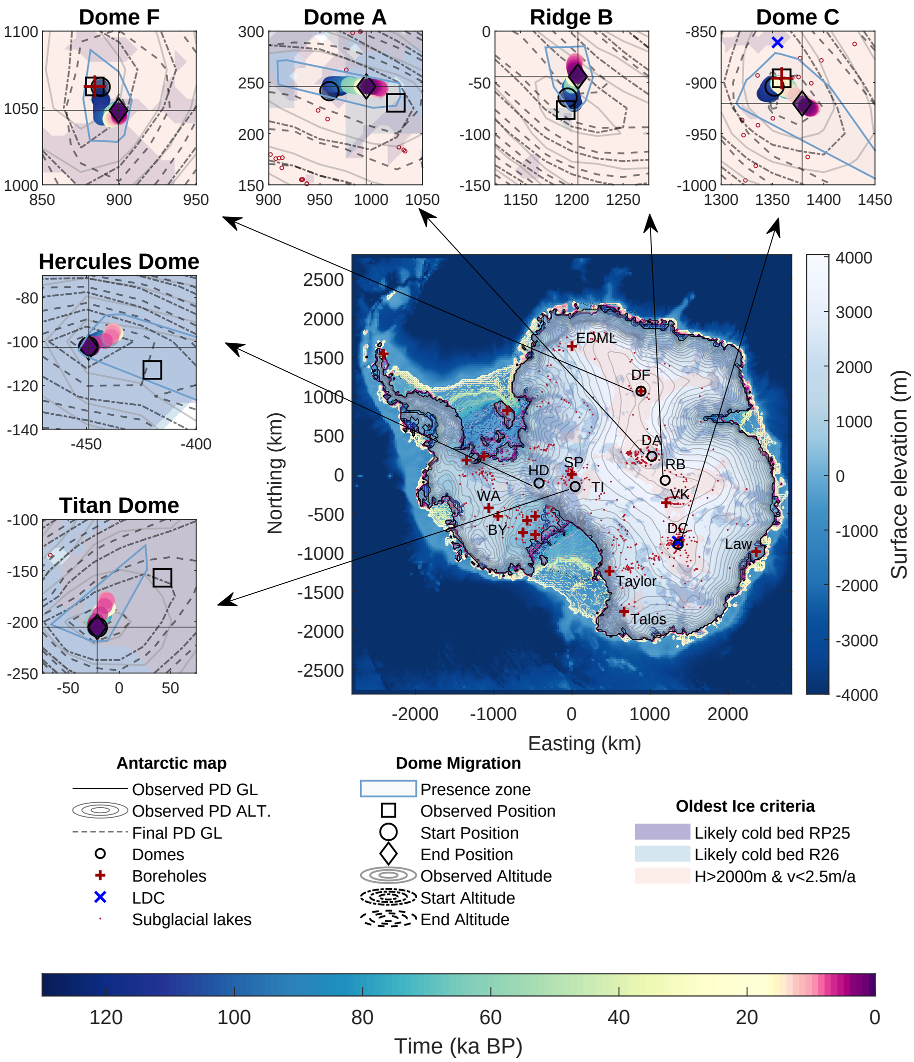

Figure 2. Evolution of Antarctic domes during the last glacial cycle. The subpanels show the migration of the domes over time (ensemble weighted-mean positions). The background of the Antarctic map represents present-day surface elevations and grounding lines (black lines) (BedMachine v3; Morlighem et al., 2020; Morlighem, 2022). The coloured lines show the evolution of the ensemble weighted-mean grounding line position over time. The grey contours outline the present-day surface elevations. The location of existing borehole measurements is indicated by red crosses. The blue cross shows the location of the Little Dome C (LDC) ice core. The shading highlights criteria favourable for preserving old ice at the base: likely cold-based areas are shown in blue (this study; R26; Raspoet et al., 2026) and purple (RP25; Raspoet and Pattyn, 2025a), areas with observed ice thickness larger than 2000 m (Morlighem et al., 2020; Morlighem, 2022) and surface velocity lower than 2.5 m a^{-1} (Mouginot et al., 2019a, b) are highlighted in light red. Note that in this study, areas are only considered as likely cold if they remained likely cold throughout the whole transient simulations. PD: present day. GL: grounding line. ALT: altitude.

https://doi.org/10.5194/egusphere-2026-5136
Preprint. Discussion started: 31 August 2026

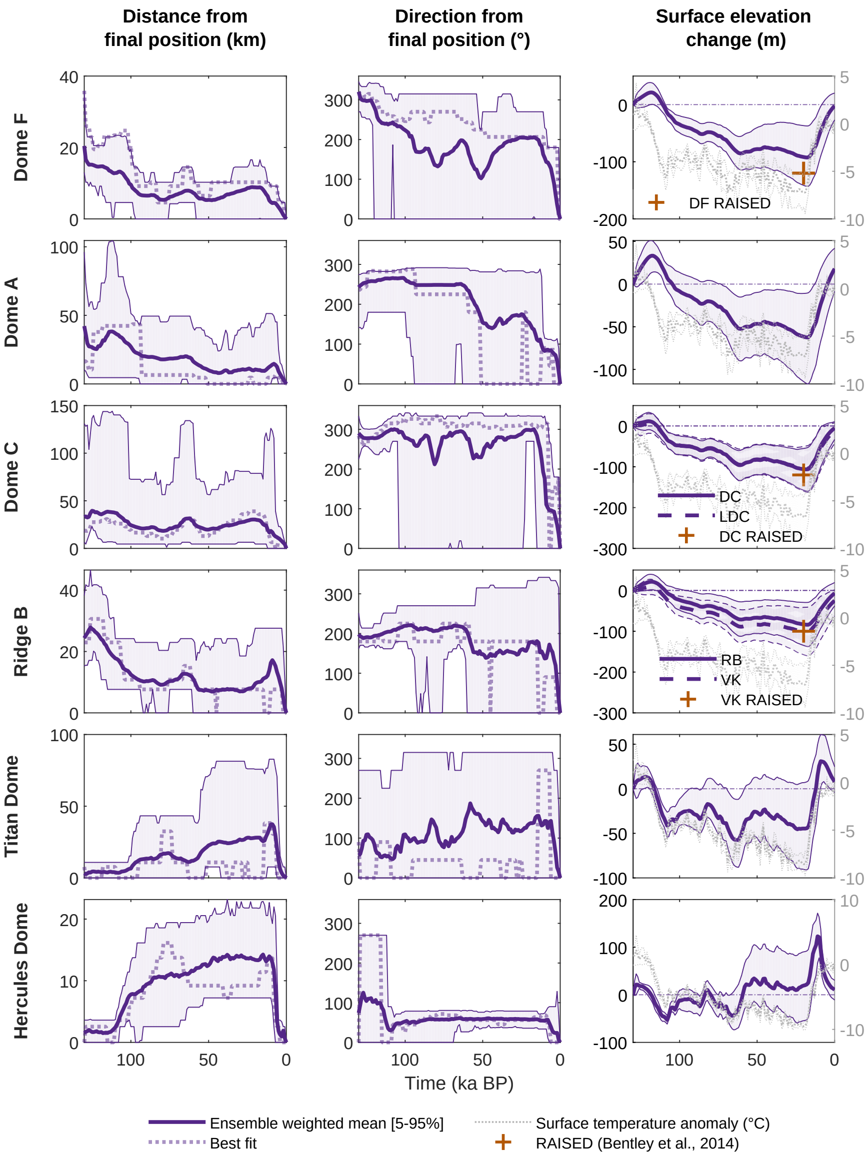

Figure 3. Change in distance, direction, and surface elevation of East Antarctic domes. Results are shown for the ensemble-weighted mean, the 5-95% ensemble-weighted spread, and the best-fit simulation. The distance and direction are determined with respect to the final modelled dome position (i.e., at 0 ka BP). Surface elevation changes are computed relative to the present-day initial state. Elevation changes reconstructions from RAISED (Bentley et al., 2014) are indicated by orange crosses. The surface temperature anomaly (°C) is highlighted in light grey. DF: Dome F. DC: Dome C. LDC: Little Dome C. RB: Ridge B. VK: Vostok.

the thermodynamic model and the climate forcing, while Dome C and Titan Dome are more sensitive to the initial climatic conditions and the climate forcing. Hercules Dome exhibits a moderate sensitivity to all factors. However, approximately one-

https://doi.org/10.5194/egusphere-2026-5136
Preprint. Discussion started: 31 August 2026

third of the total variance is attributable to interactions between factors, while another third remains unexplained (residuals). This suggests that a substantial portion of the ensemble variability is not captured by the specified factors and likely reflects higher-order interactions, nonlinear dynamics, or more complex response structures. Indeed, dome migration is primarily driven by atmospheric forcing (surface temperature and accumulation patterns), but also by grounding line advance and retreat, which can cause a reorganisation of the ice flow pattern (Figures 2, S19–S23, S27a).

As for elevation changes, they varied by 50–150 m between glacial and interglacial periods (Figure 3). For all domes, surface elevations increase slightly during the LIG, decrease gradually until reaching a minimum at the LGM, and then rise rapidly again during the Holocene. The domes of the East Antarctic plateau (i.e., Dome F, Dome A, Dome C, and Ridge B) exhibit similar lagged responses to the atmospheric forcing (Figures 3, S27b). In contrast, Titan and Hercules domes follow different patterns, likely influenced by ice-dynamical processes in West Antarctica. They also respond faster to the atmospheric forcing during the LIG and present a sharp increase in elevation around 10 ka BP in the Holocene, followed by a decrease toward the present day (Figure 3). The lag in response to climate forcing is proportional to the local ice thickness, i.e., domes with smaller ice thickness respond faster. The elevation changes are primarily controlled by local surface accumulation. Consequently, the total variance is primarily explained by the climate forcing approach (Figure S28). The elevation changes are less pronounced when simulations are forced with the climate index method than with the ice core forcing approach, because the latter produces more pronounced accumulation anomalies relative to the present day, leading to lower accumulation rates during glacial periods (Figure S29). Finally, one can note that the ensemble produces elevation changes in close agreement with the RAISED compilation (Bentley et al., 2014) for Dome F, Dome C and Vostok (Figures 3; S8b).

3.3 Evolution of basal thermal conditions

The evolution of basal thermal conditions (basal temperatures and melt rates) during the last glacial cycle is shown for each dome location in Figure 4. For all domes, basal temperatures and melt rates respond to the climate forcing with a time lag ranging from 17 to 35 ka. Therefore, the maximum and minimum basal temperatures occur after the LIG and the LGM, and the present-day basal temperatures still reflect the cooling effects from the LGM climate. The amplitude of changes in basal temperatures and melt rates varies across the domes. Dome F, Dome C, and Ridge B exhibit likely temperate basal conditions. These domes are, on average, close to thermal steady-state, with mean changes in basal temperatures and melt rates of the order of $\sim$ 0.5 °C and $\sim$0.7 mm a^{-1} during the last glacial cycle. These amplitudes are in the range of Passalacqua et al. (2017, Figure 8) for Dome C and Obase et al. (2023) for Dome F. In contrast, Titan and Hercules domes exhibit cold basal conditions in all simulations (i.e., absence of basal melt), along with a more pronounced variability in basal temperature changes ($\sim$2–5°C). Most simulations also predict cold basal conditions for Dome A, where basal temperatures varied by $\sim$ 1.5 °C during the last glacial cycle. Both the likelihood of cold basal conditions and the amplitude of changes in basal temperatures and melt rates are inversely proportional to the ice thickness at a given location (Figures 4).

On average, each of the considered regions presents at least 20% of grid cells with likely cold basal conditions (Figures 4–5). Cold basal conditions are widespread in the regions surrounding Titan Dome (88 [75–98]%), Hercules Dome (89 [83–100]%), and Dome A (72 [26–93] %). In contrast, the likelihood of temperate basal conditions is higher in the regions around Dome C

https://doi.org/10.5194/egusphere-2026-5136
Preprint. Discussion started: 31 August 2026

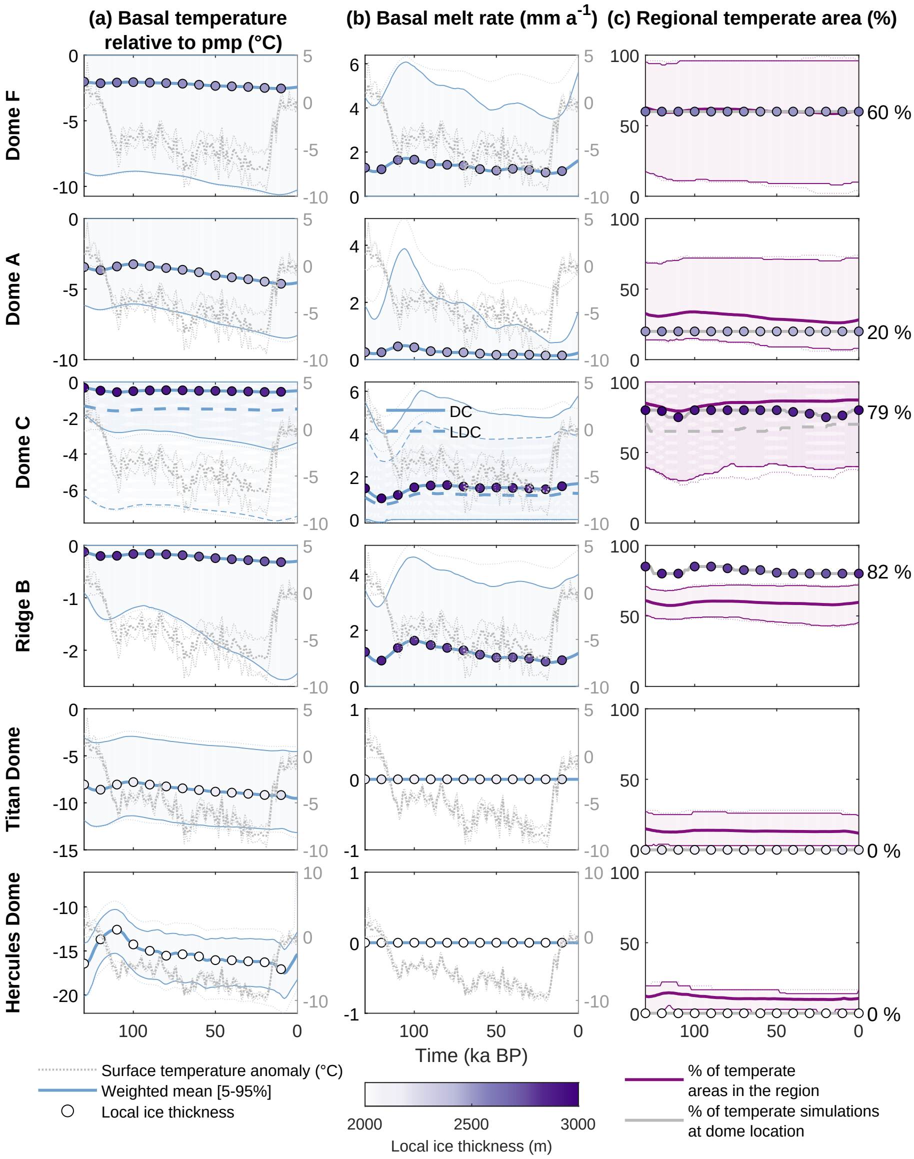

Figure 4. Evolution of basal conditions at dome locations. (a) Basal temperatures relative to the pressure melting point (pmp). The grey dotted lines show the surface temperature anomaly at a given location to illustrate the lag in the response to the forcing. The scatter plots highlight the evolution of the ensemble weighted mean ice thickness for each site. (b) Basal melt rates. (c) Regional temperate area, i.e., the percentage of temperate basal conditions in each region presented in Figure 5. The grey lines show the percentage of simulations estimating temperate basal conditions at a given dome location.

(87 [37–100] %), Dome F (60 [4–96] %), and Ridge B (59 [44–73]%). The percentage of temperate areas in a given region is mainly influenced by the GHF (> 95 %; Figure S30). For the domes of the East Antarctic plateau, > 95 % of the variability

https://doi.org/10.5194/egusphere-2026-5136
Preprint. Discussion started: 31 August 2026

in modelled basal temperatures can be ascribed to the GHF (Figure S30). For Titan Dome, the variance in basal temperatures is explained half and half by GHF and initial climatic conditions (Figure S30). For Hercules Dome, GHF explains $\sim$ 40 % of the total variance, followed by the choice of the thermodynamic model and initial climatic conditions (Figure S30). GHF contributes by 50 % to the total variance in modelled basal melt rates, which are also influenced by the choice of the thermodynamic model and interactions between factors (Figure S30).

For each of the studied regions, results for the present-day (0 ka BP) are further compared with those of Raspoet and Pattyn (2025a), who conducted an ensemble of simulations of basal and englacial thermal conditions of the AIS at 8 km resolution assuming a thermal steady-state (Figure 5). Despite the coarser resolution in the present study, our simulations capture similar basal temperature patterns to those of Raspoet and Pattyn (2025a), specifically for Dome F, Dome A, Dome C, and Ridge B, but diverge for Titan and Hercules Dome, especially for basal melt rates. These contrasts can be explained by the thermal memory associated with previous glacial-interglacial climate variability that leads to lower basal temperatures and melt rates in our palaeo simulations (e.g., Figures S2–S3, S31–S32), differences in spatial resolution, and the choice of boundary conditions and model approximations. To disentangle these effects, we conducted experiments starting from a subset of initial englacial temperatures reported by Raspoet and Pattyn (2025a), using the same model and boundary conditions, and applied a simple temperature forcing over the last 800 ka, following the initialisation procedure described in the method section (Figure S1). This significantly reduced the discrepancies between the 25 and 8 km simulations, although topographic effects remain better captured at 8 km (Figure S32). We note that our modelled basal temperatures during the previous glacial cycles never exceed those determined from the corresponding thermal steady-state initialisation (Figure S31). This suggests that thermal steady-state estimates of subglacial thermal conditions should be regarded as an upper bound, as they do not capture cooling effects from past glacial-interglacial climates.

4 Discussion

4.1 Stability of East Antarctic divide regions

The migration of East Antarctic domes and ice divides during the last glacial cycle remains poorly constrained and appears to vary substantially between sites. Early theoretical studies have demonstrated that ice divides are highly sensitive to changes in accumulation patterns, ice thickness, and boundary conditions (e.g., Hindmarsh, 1996; Nereson et al., 1998). Dome migration can be tracked by analysing radar isochrones, as even modest divide migrations can significantly influence internal stratigraphy and age-depth relationships (Hindmarsh, 1996; Martín et al., 2009). For instance, large variations in divide position can spread out Raymond arches (characteristic upward arches in internal layering formed beneath stable ice divides that reflect long-term ice flow stagnation and divide stability; Raymond, 1983; Hindmarsh, 1996), while repeated reversals in the direction of divide migration can generate multiple-folding events within the ice (Hindmarsh, 1996), with potential disruptive effects on ice cores (e.g., Hindmarsh, 1996; Wirths et al., 2026). Alternatively, a recent study (Wirths et al., 2026) has investigated the influence of ice sheet surface elevation and ice divide variability on ice-core-based climate reconstructions using three ice-sheet model simulations spanning the MPT. Here, we analyse dome migration patterns derived from an ensemble of transient simulations

https://doi.org/10.5194/egusphere-2026-5136
Preprint. Discussion started: 31 August 2026

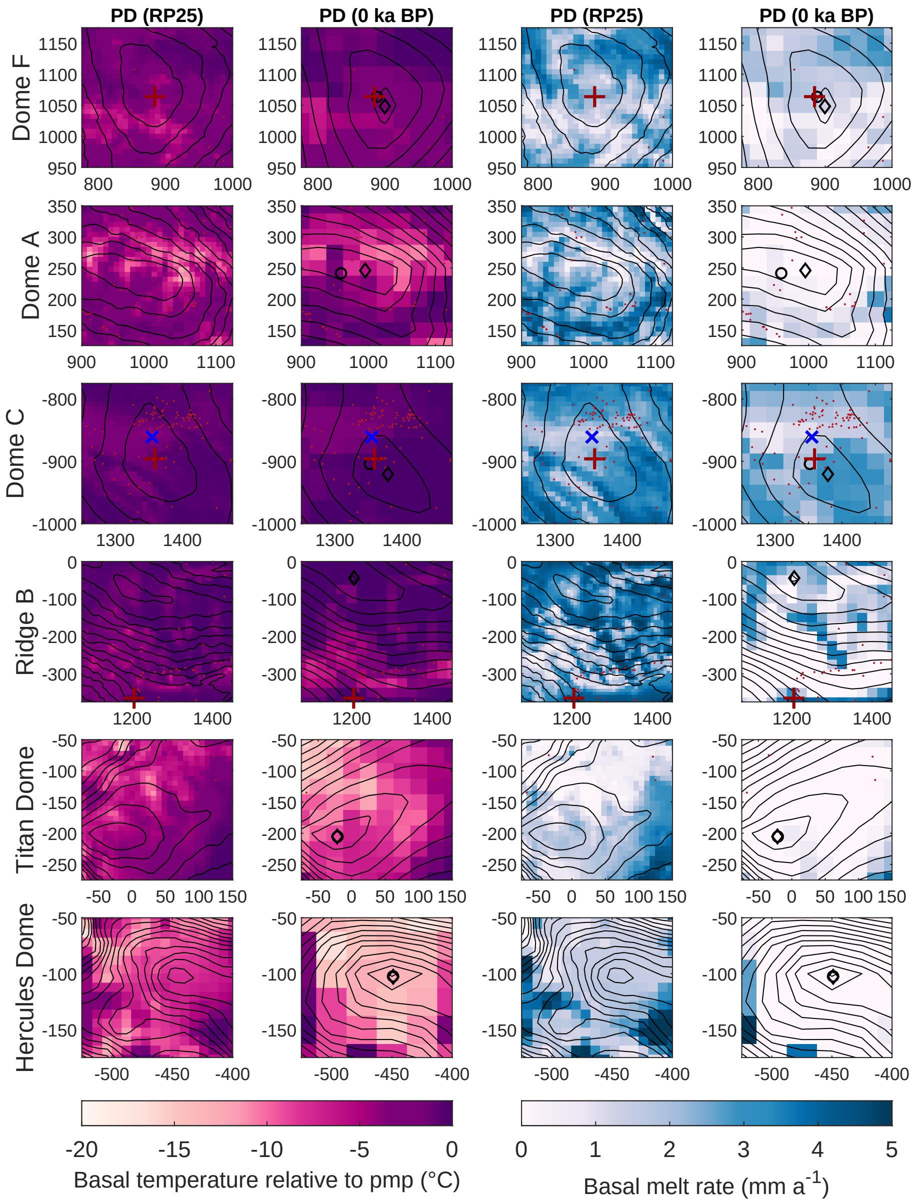

Figure 5. Comparison of modelled basal temperatures and melt rates at 0 ka BP with the results of Raspoet and Pattyn (2025a, RP25). Values for basal temperatures are truncated between -20 and 0°C while values for basal melt rates are truncated between 0 and 5 mm a^{-1}. Results of this study are shown for the ensemble-weighted mean. Differences between the two include the spatial resolution (25 and 8 km), choice of boundary conditions, model approximations, and thermal steady-state assumption in RP25. The location of boreholes are indicated by red crosses, the location of the LDC is shown by a blue cross, and subglacial lakes are highlighted by small red circles. The black circles and diamonds highlight initial and final modelled weighted mean dome positions, respectively.

https://doi.org/10.5194/egusphere-2026-5136
Preprint. Discussion started: 31 August 2026

of the AIS over the last glacial cycle, enabling assessment of both local drivers, such as accumulation changes, and large-scale ice-sheet processes, including grounding-line retreat.

Model results indicate no substantial ice-divide migration over the last glacial cycle, with average dome displacements limited to 20–40 km from present-day positions. Our modelled dome displacements are comparable in amplitude to those reported in a recent modelling study (Wirths et al., 2026). This finding is also consistent with airborne radar surveys that reveal laterally continuous, undisturbed internal isochrones around Dome F (e.g., Steinhage et al., 2013), and with the continuity of internal isochrones and basal freeze-on reflectors at Dome A, which suggest stability for at least one and a half glacial cycles (Wolovick et al., 2021a). Although variations in accumulation are observed across and along Ridge B (Leysinger Vieli et al., 2004), no radar-stratigraphic evidence for substantial divide migration has been reported. Radar stratigraphy and ice-flow measurements at Hercules Dome also indicate a stable ice divide, characterised by continuous internal layering and a frozen-bed regime, supporting minimal divide migration over at least the last glacial cycle (Hills et al., 2025). In contrast, our model results for Dome C reveal a more complex migration pattern. While radar isochrones indicate steady ice flow and accumulation over the past 100 ka (Siegert et al., 2001), recent observations show slight variations in accumulation patterns over centennial timescales (Urbini et al., 2008), along with significant summit migration on decadal timescales (Vittuari et al., 2025). Our results indicate only minor displacement and no major ice-flow reorganisation in the region surrounding Titan Dome. However, radar stratigraphy reveals evidence of past ice-flow reorganisation, suggesting that ice-divide migration may have occurred at Titan Dome (Beem et al., 2018, 2021). We find elevation changes of the order of 50–150 m between glacial and interglacial periods, in agreement with previous modelling studies (Ritz et al., 2001; Wirths et al., 2026) and palaeo-reconstructions (Bentley et al., 2014). The elevation changes at the domes exhibit a lagged response to climate forcing proportional to local ice thickness and are primarily driven by variations in local precipitation patterns.

The glacial-interglacial model experiments demonstrate that dome migrations are influenced by grounding line advance during glacial periods, combined with changes in the precipitation regime across the divide areas. While our simulations do not exhibit significant grounding line retreat during the LIG, some Antarctic basins may have been prone to significant grounding line retreat and potential WAIS collapse during warmer interglacial periods (e.g., Bentley and Wolff, 2026), which may have a significant impact on the stability and position of the domes and divides. We investigate the sensitivity of dome trajectories to extensive grounding-line retreat using existing long-term (i.e., millennial-to-multi-millennial) projections performed with the Kori-ULB model by Coulon et al. (2024) and Klose et al. (2024) under SSP1-2.6 and SSP5-8.5 scenarios (Figures S38–S39). The SSP1-2.6 scenario leads to a partial collapse of the Thwaites Glacier in West Antarctica, along with retreat of the grounding line in the Wilkes subglacial basin on centennial timescales. Such grounding-line retreat is associated with small dome displacements of a few tens of kilometres from the present-day positions, along with negligible elevation changes (Figure S39). This scenario is the most representative of past interglacial periods, with warming levels slightly below the LIG. However, under the SSP5-8.5 scenario, significant warming is projected, which leads to the collapse of the WAIS, Wilkes, and Recovery subglacial basins (Figure S38). This can drive significant dome displacements of the order of 100 km and dome elevation changes of several hundred meters (Figure S39). Nevertheless, the SSP5.8-5 scenario is associated with much larger

https://doi.org/10.5194/egusphere-2026-5136
Preprint. Discussion started: 31 August 2026

warming levels than experienced over the last 800 ka (Jouzel et al., 2007), making such collapses very unlikely during previous interglacial periods.

4.2 Basal thermal conditions and thermal memory

We find heterogeneous basal thermal conditions beneath the studied East Antarctic domes. The regions surrounding Titan Dome, Hercules Dome, and Dome A exhibit likely cold basal conditions, whereas the region around Dome C is predominantly temperate at the base, except near the LDC drilling site (Figure 5). A frozen bed patch is also expected between Ridge B and Vostok (Figure 5). Basal conditions in the Dome F and Dome C regions are sensitive to the GHF, which vary substantially across the study areas and among the GHF datasets (Figure S33). The Stål et al. (2021) and Shen et al. (2020) GHF datasets yield significantly colder basal environments, with absence of basal melting (Figures S34–S35), but they also predict cold basal conditions in regions where subglacial lakes are expected (Figures S34–S35). In contrast, similar basal temperatures and melt rates are simulated for Dome A, Ridge B, Titan Dome, and Hercules Dome despite differences among GHF datasets (Figure S33), as local topographic features exert more influence on basal thermal conditions in these regions (Figures S34–S35). In addition, as discussed by Sutter et al. (2019), dome displacement can also be influenced, to a certain extent, by the GHF distribution (Figures S30; S34–S35). Because of the relevance for both ice dynamics and old ice research, several efforts have been made to better constrain GHF and basal conditions in these regions using radar data (e.g., Passalacqua et al., 2017; Jordan et al., 2018; Wolovick et al., 2021a, b; Wang et al., 2023b; Lang et al., 2025; Kerr et al., 2026).

Existing continental-scale GHF datasets vary widely in both amplitude and spatial distribution (Burton-Johnson et al., 2020; Reading et al., 2022) and show poor agreement with radar-derived estimates (e.g., Wolovick et al., 2021a; Lang et al., 2025; Kerr et al., 2026) as they fail to resolve small-scale anomalies and spatial heterogeneities (Carson et al., 2013), which could affect basal thermal conditions in the investigated regions. As a result, at some locations such as Dome F, none of the GHF datasets aligns with borehole-derived values (Talalay et al., 2020), leading to divergent estimates of basal temperatures and melt rates (Figures S36–S37). In addition, we also overestimate the basal temperature at LDC, where a recent borehole measurement inferred a basal temperature of approximately -8°C (Westhoff et al., 2026). In contrast, the ensemble mean basal temperature at 0 ka BP for LDC is -4 [-10.2 – -4.5] °C (not corrected for the pressure melting point), and ∼70% of our simulations estimate temperate basal conditions at this site, despite GHF values (42–58 mW m^{-2}) being close to the inferred value (51 ± 5 mW m^{-2}). This discrepancy results from an overestimation of the modelled ice thickness (2978–3063 m) compared to the observed ice thickness (2800 m), which acts as an insulator and affects the pressure melting point of ice, so that a lower GHF would be required to maintain cold basal conditions (e.g., Figure 2 in Van Liefferinge and Pattyn, 2013). Similar discrepancies between modelled and measured ice thicknesses can be observed at other sites as well and likely result from the coarse resolution of our model simulations, which may account for some model-data differences (Figure S36).

We observe a progressive cooling trend in the modelled basal temperatures (Figure 4), which reflects the long-term thermal inertia of the ice sheet (Figures S2–S3). The basal temperature of the studied domes responds to the climate forcing with a time lag of ∼ 17–35 ka. This effect is more pronounced over Hercules Dome, Titan Dome, and Dome A, while Dome F and Dome C seem closer to a thermal steady state (Figures S3; S31–S32). The time lag and amplitude of changes depend on the

https://doi.org/10.5194/egusphere-2026-5136
Preprint. Discussion started: 31 August 2026

local ice thickness, with thicker ice favouring longer and dampened responses. However, we prescribe a constant geothermal boundary condition that does not evolve with the basal thermal state. We therefore neglect conductive heat transfer within the underlying bedrock and account only for the thermodynamic evolution in the ice column. This may reduce the lithospheric thermal memory and shorten the response time of basal temperatures to climate forcing. As a result, our modelled temperature fields may adjust more rapidly and respond with larger amplitude than would a fully coupled ice-bedrock thermal system (e.g., Ritz, 1987, 1992). Nevertheless, the ensemble of modelled temperature profiles at 0 ka BP aligns well with borehole measurements within the model uncertainty bounds (Figures S3 and S9), although only simulations using the enthalpy model reproduce basal melt rates in the range of the borehole-derived estimates of Talalay et al. (2020) (Figure S37).

4.3 Implications for oldest ice

Overall, the evolution of dome position and basal thermal conditions constitute key constraints for the preservation of old ice and localisation of suitable drilling sites. Such sites are associated with cold basal conditions (absence of basal melting), thick ice, low ice-flow speeds and limited dome migration, which together minimise stratigraphic disturbance (Fischer et al., 2013; Parrenin et al., 2017). Since our modelled basal temperatures and melt rates never exceed the present-day thermal steady-state values during the last glacial cycle, we can use the higher resolution estimates of Raspoet and Pattyn (2025a) as an upper bound to estimate likely cold basal conditions for the AIS. Combined with observed topographic (Morlighem et al., 2020; Morlighem, 2022) and velocity data (Mouginot et al., 2019a, b), we can derive an updated map of promising oldest ice sites similar to Van Liefferinge and Pattyn (2013), considering that our experiments have shown that most divide locations remain relatively stable in time. We also exclude grid cells where subglacial lakes are expected (Livingstone et al., 2022). Results are presented in Figure 6. Overall, our potential old ice sites are similar to Van Liefferinge and Pattyn (2013) and Sutter et al. (2019) but cover smaller areas. We find candidate sites in all five regions except Hercules Dome, where the ice thickness is too low. While Dome Fuji, Dome C, Ridge B, and Dome A are well-established candidates for the preservation of old ice (e.g., Van Liefferinge and Pattyn, 2013; Sutter et al., 2019), the suitability of Titan Dome is more debated, due to potential variability in past ice-flow dynamics, the possibility that basal ice is too young, and insufficient temporal resolution to resolve older ice layers (Beem et al., 2021). Our findings support ongoing investigations, and future work combining ice-flow modelling with high-resolution radar surveys will be essential to further evaluate and refine the identification of potential old ice sites.

5 Conclusions

We present an ensemble of transient thermomechanical simulations of the Antarctic Ice Sheet spanning the last glacial cycle, using an initialisation procedure that minimises ice thickness misfits while capturing long-term thermal memory effects. The ensemble is evaluated against a comprehensive set of observational and geological constraints covering both past and present-day ice-sheet configurations. This ensemble is used to examine the stability of six domes and divide regions within the EAIS, along with the evolution of their subglacial conditions. Unlike most palaeo-ice-sheet modelling studies, which rely on long-term or palaeo spin-up initialisations, our approach accurately captures the initial ice sheet configuration, resulting in modelled

https://doi.org/10.5194/egusphere-2026-5136
Preprint. Discussion started: 31 August 2026

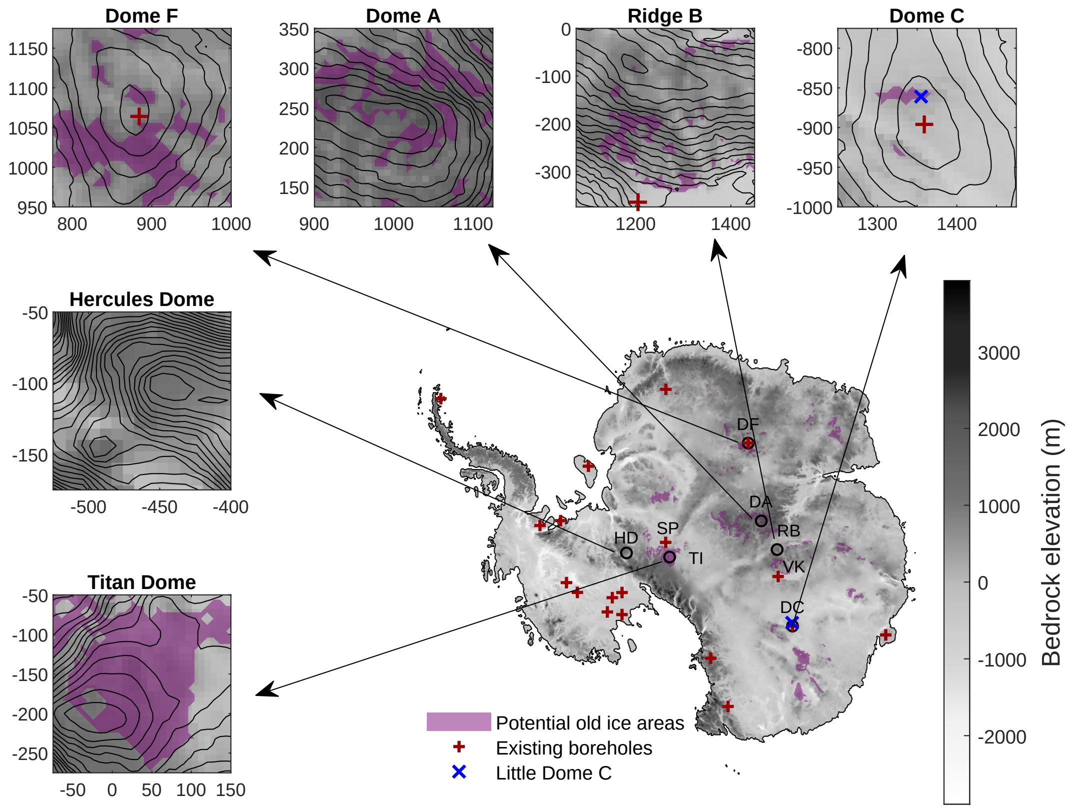

Figure 6. Potential old ice sites in the studied regions. Promising old ice sites are outlined in dark pink. These are defined as likely cold basal conditions in this study and in Raspoet and Pattyn (2025a), ice thickness > 2000 m, and ice velocities < 2.5 m a^{-1} (see Figure 2). Existing deep boreholes are represented by red crosses, and the location of the recently drilled ice core at LDC is represented by a blue cross. The black contours delineate present-day surface elevations. The background shows the bedrock elevation. Topographic data are from BedMachine v3 (Morlighem et al., 2020; Morlighem, 2022).

dome positions that align with observed locations. We also provide an updated assessment of areas with favourable conditions for the preservation of old ice at the base, which may be targeted in future drilling campaigns. Additionally, our findings can inform corrections of isotope data retrieved from ice-core records for local ice elevation changes and upstream effects associated with past dome displacements.

Results suggest that EAIS domes and divides remained relatively stable throughout the last glacial cycle, with migrations generally limited to within 20–40 km of their initial positions. Dome migration is primarily controlled by variations in local accumulation patterns and large-scale grounding-line migration during the glaciation, although GHF also exerts an influence, particularly for Dome F and Dome A. The overall stability of the domes is associated with the absence of substantial grounding-line retreat in the EAIS during the LIG in our model simulations. Surface elevation changes exhibit a lagged response to climate forcing and range from 50 to 150 m across the East Antarctic Plateau between glacial and interglacial periods, with lower

https://doi.org/10.5194/egusphere-2026-5136
Preprint. Discussion started: 31 August 2026

elevations corresponding to reduced accumulation rates during the LGM and a lagged response that is proportional to dome ice thickness.

Basal temperatures and melt rates show a delayed response to climatic forcing by approximately 17–35 ka, indicating that present-day basal thermal conditions continue to reflect the colder LGM climate. Consequently, estimates from simulations assuming a thermal steady state should be regarded as an upper bound of the present-day thermal regime. The probability of cold basal conditions is highest in the regions surrounding Hercules Dome, Titan Dome, and Dome A. However, estimates of the basal thermal state are highly sensitive to GHF and errors in modelled ice thickness of a few hundred meters. We identify potential sites for oldest ice in all investigated regions except Hercules Dome, where ice thickness is insufficient. The identified sites are consistent with previous studies (Van Liefferinge and Pattyn, 2013; Sutter et al., 2019), although spread over smaller areas. Future work using high-resolution radar surveys could help better constrain the conditions at the ice-bedrock interface in these regions.

Code and data availability. The codes used to run the Kori-ULB model and produce the figures, as well as data supporting the results presented in this study are available on Zenodo: https://doi.org/10.5281/zenodo.22047132 (Raspoet et al., 2026). Results from Raspoet and Pattyn (2025a) are available at: https://doi.org/10.5281/zenodo.15664172 (Raspoet and Pattyn, 2025b). The code and reference manual of the Kori-ULB ice-sheet model are publicly available on https://github.com/FrankPat/Kori-ULB. All datasets used in this study are freely accessible through their original references. Additional information can be provided upon request from the authors.

Appendix A: List of key model parameters

Table A1 presents a non-exhaustive list of model parameters used in the Kori-ULB ice sheet model and their values in this study.

https://doi.org/10.5194/egusphere-2026-5136
Preprint. Discussion started: 31 August 2026

Table A1. List of key model parameters.

Symbol	Description	Value	Units
Ice dynamics			
m	Basal sliding exponent	3	-
n	Flow law exponent	3	-
ρ_i	Ice density	917	kg m^{-3}
ρ_w	Sea water density	1027	kg m^{-3}
ρ_f	Fresh water density	1000	kg m^{-3}
ρ_*	Reference density in EOS	1033	kg m^{-3}
Ice thermodynamics			
β	Clausius-Clapeyron gradient	8.66×10^{-4}	K m^{-1}
c_p	Heat capacity of ice	2009	J kg^{-1} K^{-1}
c_{p0}	Heat capacity of sea water	3974	J kg $^{-1}$ °C^{-1}
$H_w^{\max}$	Maximum water layer thickness in the enthalpy model	2	m
K	Conductivity of ice	2.1	W m^{-1} K^{-1}
K_c	Diffusivity of cold ice in the enthalpy model	K/c_p	kg m^{-1} s^{-1}
K_0	Diffusivity of temperate ice in the enthalpy model	$K_c \times 10^{-5}$	kg m^{-1} s^{-1}
L	Latent heat of fusion	3.35×10^5	J kg $^{-1}$
T_0	Absolute melting point of ice	273.15	K
T_{ref}	Reference temperature in the enthalpy model	223.15	K
PDD model			
γ_{atm}	Atmospheric lapse rate	-0.008	°C m^{-1}
d_{ice}	Thickness of the thermally active layer	5	m
K_{ice}	Degree-day factor for the melting of ice	$8/\rho_i$	w.e. mm PDD^{-1}
K_{snow}	Degree-day factor for the melting of snow	$3/\rho_i$	w.e. mm PDD^{-1}
Tuning parameters for the PICO model (Reese et al., 2018)			
C	Overturning strength of ocean circulation underneath ice shelf	1×10^6	m^3 s^{-1}
γ_T^*	Effective turbulent temperature exchange velocity	2×10^{-5}	m s^{-1}
Tuning parameters for the climate forcing			
F_P	Sensitivity factor for precipitation change with temperature	0.053	°C^{-1}
F_M	Sensitivity factor for ocean temperature change with atmospheric temperature	0.25	-

https://doi.org/10.5194/egusphere-2026-5136
Preprint. Discussion started: 31 August 2026

Appendix B: Scoring and weighting of the ice-sheet model outputs

This appendix presents the methodology used to score and weight ensemble members based on their ability to reproduce a set of past and present-day observational and geological constraints. We closely follow the approaches described in Pollard et al. (2016) and Albrecht et al. (2020b) and use their terminology when applicable, but make use of more recent observational datasets for both present-day observations and past ice-sheet reconstructions. The model results are evaluated against 11 data types using mean squared errors (MSE), as described in Appendix B1. Each misfit ($M_{i,j}$) is then normalised into individual scores ($S_{i,j}$) that are combined into one aggregated score (S_j) for each ensemble member j (Pollard et al., 2016), as detailed in Appendix B2.

B1 Evaluation of model misfits

We evaluate our model results against both present-day constraints and past ice sheet reconstructions. The first set of constraints is given by the present-day Antarctic ice sheet geometry (thickness and grounding-line position) and velocity field (MEaSUREs BedMachine v3 and Phase-Based Antarctica Ice Velocity Map v1; Morlighem et al., 2020; Morlighem, 2022; Mouginot et al., 2019a, b). All gridded datasets are resampled at our 25 km model resolution.

1. TOTE: total area of model–data mismatch for grounded ice (Pollard et al., 2016; Albrecht et al., 2020b). Misfit $M_1 = (A/B)^2$ where $B = (A_{tot})^{1/2}\sigma_w$, A is the total area of mismatch between modelled and observed grounded ice, A_{tot} is the total area of the domain, σ_w = 30 km represents the typical size of modern grounding-line location errors in "reasonable" model runs (Pollard et al., 2016, Appendix B1). The continental domain is defined by bed elevation above -2500m (Albrecht et al., 2020b). Data: BedMachine v3 (Morlighem et al., 2020; Morlighem, 2022).

2. TOTI: total area of model–data mismatch for floating ice (Pollard et al., 2016; Albrecht et al., 2020b). Misfit $M_2 = (A/B)^2$ where $B = (A_{tot})^{1/2}\sigma_w$, A is the total area of mismatch between modelled and observed floating ice (i.e., ice-shelf areas), A_{tot} is the total area of the domain, σ_w = 30 km represents grounding-line and calving front location uncertainty in "reasonable" model runs (Pollard et al., 2016, Appendix B2). Data: BedMachine v3 (Morlighem et al., 2020; Morlighem, 2022).

3. TOTDH: model–data differences for grounded ice thickness (Pollard et al., 2016; Albrecht et al., 2020b). Misfit $M_3 = \mathrm{mean}((h - h_{obs})/\sigma_h)^2$ where h is the modelled ice thickness, h_{obs} is the observed ice thickness, and σ_h = 10 m is an assumed uncertainty in "reasonable" model runs. The mean is taken over areas with present-day observed grounded ice. Data: BedMachine v3 (Morlighem et al., 2020; Morlighem, 2022). Model misfits are presented in Figure S7.

4. TOTGL: model-data differences in grounding-line location (Albrecht et al., 2020b). Misfit $M_4 = \mathrm{mean}((d - d_{obs})/\sigma_d)^2$, where d and d_{obs} are the distances from the modelled and observed grounding lines (e.g., $d = 0$ at the modelled grounding line location), respectively, calculated using a two dimensional distance field approximation, and σ_d = 30 km is the assumed uncertainty in grounding line location as in TOTI and TOTE (Albrecht et al., 2020b). This method is close to

https://doi.org/10.5194/egusphere-2026-5136
Preprint. Discussion started: 31 August 2026

the misfit described in Albrecht et al. (2020b) but different from the GL2D misfit used in Pollard et al. (2016, Appendix B5). Data: BedMachine v3 (Morlighem et al., 2020; Morlighem, 2022).

5. TOTVEL: model-data differences in surface ice velocity over grounded ice (Albrecht et al., 2020b). Misfit $M_5 = \mathrm{mean}((v - vobs)/\sigma_v)^2$, where v is the modelled velocity, v_{obs} is the observed velocity, and σ_v is the observational error in the observational velocity. This is close to Albrecht et al. (2020b), although we evaluate the misfits for each horizontal velocity component (x and y) rather than speed, and sum the resulting contributions. Data: Phase-Based Antarctica Ice Velocity Map v1 (Mouginot et al., 2019a, b). Model misfits are presented in Figure S7.

The second set of constraints is provided by the reconstruction of the Antarctic ice sheet deglaciation (RAISED consortium; Bentley et al., 2014), which compiles a range of observational constraints for four key time slices during the deglaciation of the Antarctic ice sheet (i.e., 20, 15, 10, and 5ka BP). Model misfits with respect to the RAISED reconstructions are presented in Figure S8.

6. DGL: model-data differences in past grounding-line positions. We employ a grounding-line distance metric analogous to TOTGL to quantify the misfit between modelled and reconstructed past grounding-line positions, leading to $M_6 = \mathrm{mean}((d - d_{obs})/\sigma_d)^2$, where d and d_{obs} are the distances from the modelled and reconstructed grounding lines, respectively, calculated using a two dimensional distance field approximation (Albrecht et al., 2020b), and σ_d = 100 km is a representative width scale of reasonable past grounding-zone mismatches (Pollard et al., 2016). This differs from both the GL2D and THROUGH formulations in Pollard et al. (2016) and Albrecht et al. (2020b). We consider the two scenarios (A and B) provided by the RAISED consortium for grounding line reconstructions as equally plausible and compute the misfits for both cases, retaining the minimum misfit. We do not restrict the analysis to specific regions but to where observations are available, and select model outputs corresponding to the closest observational time slices.

7. DSURF: model-data differences in past elevation changes. Similar to Pollard et al. (2016), we select for each data point a time series of model surface elevation changes within a window time defined by the observational time uncertainty ($\tau \in [t_{obs} \pm \sigma_t]$) at the closest model grid point of the measurement and consider the minimum absolute difference over all model times. Here, we chose σ_t = 500 years around a given time slice and σ_{h_s} = 100 m for the surface elevation uncertainty. The mean over all data points leads to misfit $M7 = \mathrm{mean}(\min_\tau |h_s(\tau) - h_{s_{obs})}|/\sigma_{h_s})^2$, where $h_s(\tau)$ is the modelled surface elevation changes within the considered time window and $h_{s_{obs}}$ is the reconstructed surface elevation change at time t_{obs}. To mitigate the influence of nearby, potentially correlated observations, the mean is computed over all data points using intra-data weighting (Briggs and Tarasov, 2013) that is inversely proportional to local sampling density, defined by the number of measurements within a distance L = 550 km of each other, ensuring equal contribution from each L-sized cluster to the overall mean (Pollard et al., 2016).

The last set of constraints is given by the Antarctic Ice Sheet palaeo-constraint database (AntICE2; Lecavalier et al., 2023, 2022). The AntICE2 database constitutes the most comprehensive observational constraint dataset available for calibrating models of the Antarctic Ice Sheet throughout the last glacial cycle. This curated dataset contains high-quality data

https://doi.org/10.5194/egusphere-2026-5136
Preprint. Discussion started: 31 August 2026

organised into specified quality tiers and represents a significant expansion of the foundational work by Briggs and Tarasov (2013).

8. ELEV: model-data differences of past surface elevations (PaleoH). The misfit is computed similarly to DSURF: $M8 = \mathrm{mean}(\min_\tau |h_s(\tau) - h_{s_{obs}}|/\sigma_{h_s})^2$, where $h_s(\tau)$ is the modelled surface elevations within the considered time window ($\tau \in [t_{obs} \pm \sigma_t]$) and $h_{s_{obs}}$ is the reconstructed surface elevation at time t_{obs}. Here, σ_t and σ_{h_s} are defined by the age and elevation uncertainties provided for each data point by the AntICE2 database. The mean over all data points is weighted by intra-data-type weighting, as described above, in combination with the tier-type quality classification associated with each data point. Note that this approach differs from the ELEV misfit described in Pollard et al. (2016) and Albrecht et al. (2020b), where the smallest misfit to observations is computed for all past ice surface elevations that are part of a thinning trend. Model misfits are presented in Figure S9.

9. EXT: model-data differences of past ice-sheet extent (PaleoExt). The PaleoExt database contains proxy records representing proximal-to-grounding-line (PGL), sub-ice-shelf (SIS), and open-marine conditions (OMCs) (Lecavalier et al., 2023; Lecavalier and Tarasov, 2025). Model-data comparison is performed by translating simulated ice-sheet states into those categorical classes for the nearest grid point to each observational constraint, within a time window defined by the observational age uncertainty ($t_{obs} \pm \sigma_t$). An observation is considered satisfied if the simulated class matches the proxy interpretation at least once within the time window. A binary misfit is then assigned to each observation (0 if satisfied, 1 if not). The overall misfit $M9$ is obtained through the weighted mean across all data points, combining the intra-data-type weighting scheme described above and the tier-type quality classification associated with each data point. This misfit represents the fraction of observations that are not reproduced by a simulation. Note that this metric differs from EXT described in Albrecht et al. (2020b). Model misfits are shown in Figure S9.

10. UPL: model-data differences in modern uplift rates (Pollard et al., 2016; Albrecht et al., 2020b). This misfit is computed as $M10 = \mathrm{mean}((U_{mod} - U_{obs})/\sigma_U)^2$, where U_{mod} and U_{obs} are modelled and observed uplift rates and σ_U is the uplift rate standard deviation given by the AntICE2 database. The mean over all data points is weighted by intra-data-type weighting, as described above, in combination with the tier-type quality classification associated with each data point. Model misfits are presented in Figure S10.

11. TEMP: model-data differences between modelled temperature profiles and borehole measurements. For each temperature profile, the misfit is computed as $M11 = \mathrm{mean}((T_{mod} - T_{obs})/\sigma_T)^2$, where T_{mod} and T_{obs} are modelled and measured temperature profiles. We chose a σ_T = 0.1°C, which represents the lowest accuracy among several borehole measurements (e.g., Talalay et al., 2020). Modelled and measured temperature profiles are interpolated on the same depth-normalised vertical grid. The mean is taken across all temperature profiles and weighted by the intra-data-type weighting described above, combined with the tier-type quality classification associated with each borehole measurement provided by the AntICE2 database. Model misfits are presented in Figure S11. A qualitative comparison between modelled and measured temperature profiles is also provided in Figure S3.

https://doi.org/10.5194/egusphere-2026-5136
Preprint. Discussion started: 31 August 2026

B2 Score aggregation

The scores are aggregated following closely the "simple averaging method" described in Albrecht et al. (2020b, Sect. 2.3) and
570 Pollard et al. (2016, Sect. 2.4.1, Approach A). Individual misfits (described above) are normalised into an individual score $S_{i,j}$ for every data type i and ensemble member j, using the median over all misfits $M_{i,j}$

$$S_{i,j} = \exp(-M_{i,j}/\mathrm{median}_j(M_{i,j}))) \,. \tag{B1}$$

Following Pollard et al. (2016) and Albrecht et al. (2020b), we assume equal importance across all data types in the overall score, thereby avoiding the inter-data-type weighting scheme of Briggs and Tarasov (2013) and Briggs et al. (2014).
575 The inter–data-type weighting scheme would favour observational constraints with higher spatio-temporal density and hence present-day constraints. The aggregate score for each simulation j is defined as the product of the scores for each data type:

$$S_j = \prod_{i=1} S_{i,j} \,. \tag{B2}$$

Finally, the scores for each ensemble member are normalised to create a weight w (Coulon et al., 2024):

$$w_j = \frac{S_j}{\sum S_j} \,. \tag{B3}$$

580 The weights obtained for each ensemble member are illustrated in Figure B1.

https://doi.org/10.5194/egusphere-2026-5136
Preprint. Discussion started: 31 August 2026

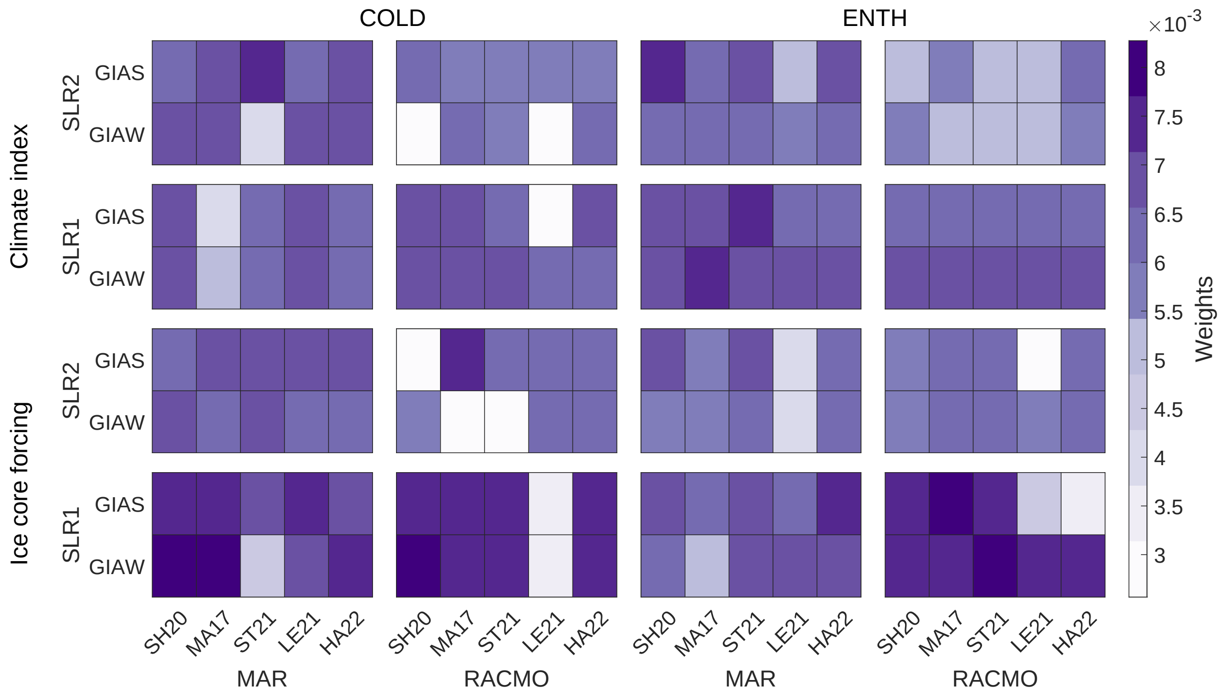

Figure B1. Weights assigned to the ensemble of simulations based on the model-observation comparison. SLR1 and SLR2 correspond to the sea level forcing derived from Spratt and Lisiecki (2016) and Bintanja and Van de Wal (2008), respectively. SH20, MA17, ST21, LE21, and HA22 refer, in order, to geothermal heat flow datasets from Shen et al. (2020), Martos et al. (2017), Stål et al. (2021), Lösing and Ebbing (2021), and Haeger et al. (2022). COLD and ENTH denote the thermodynamic models (cold-ice and enthalpy methods, respectively). The factors of uncertainty and corresponding references are presented in Table 1. Higher weights are associated with simulations demonstrating better agreement with observations.

Appendix C: Variance-based sensitivity analysis

To quantify the sensitivity of model simulations to the various factors of uncertainty considered in this study (Table 1), we perform a variance-based sensitivity analysis using analysis of variance (ANOVA; Girden, 1992; Von Storch and Zwiers, 2002), following the approaches of Seroussi et al. (2024) and Coulon et al. (2025). This statistical technique allows us to partition the total variance in model outputs into contributions from individual uncertainty factors by comparing group means and assessing if statistically significant differences exist between them. The method captures both the variance explained by main effects, which arise from each factor independently, and the variance due to interactions between factors. Interactions represent the portion of variance that cannot be assigned to any single factor, as certain effects emerge only when multiple factors are varied simultaneously. Thus, interactions quantify the variance attributable to the combined influence of two uncertainty factors. Consistent with Coulon et al. (2025), we conduct a Type-I sequential ANOVA on the weighted model ensemble using linear regression models and compute variance contributions using weighted sums of squares, thereby enabling incremental

https://doi.org/10.5194/egusphere-2026-5136
Preprint. Discussion started: 31 August 2026

attribution of variance to each factor. Although additional two-way interactions, higher-order interactions involving three or more parameters, and unexplained residual variance may also contribute to the variance (Coulon et al., 2025), these are not analysed explicitly in this study.

Author contributions. OR and FP conceived the study. OR designed the experiments, performed the simulations, conducted the analysis, interpreted the results, and wrote the first draft of the manuscript with the help of VC and FP. All authors contributed to writing and revising the final manuscript.

Competing interests. The authors declare that they have no conflict of interest.

Acknowledgements. This publication was generated in the frame of Beyond EPICA. The project has received funding from the European Union's Horizon 2020 research and innovation programme under grant agreement nos. 730258 (Oldest Ice) and 815384 (Oldest Ice Core). It is supported by national partners and funding agencies in Belgium, Denmark, France, Germany, Italy, Norway, Sweden, Switzerland, the Netherlands and the United Kingdom. This is Beyond EPICA publication number XX. Computational resources have been provided by the Consortium des Équipements de Calcul Intensif (CÉCI), funded by the Fonds de la Recherche Scientifique de Belgique (F.R.S.-FNRS) under Grant No. 2.5020.11 and by the Walloon Region. O. R. is a FRIA grantee of the Fonds de la Recherche Scientifique de Belgique (F.R.S.-FNRS). V.C. acknowledges funding by the Fonds de la Recherche Scientifique de Belgique (F.R.S.-FNRS) with an F.R.S.-FNRS Postdoctoral Researcher Fellowship.

References

Albrecht, T., Winkelmann, R., and Levermann, A.: Glacial-cycle simulations of the Antarctic Ice Sheet with the Parallel Ice Sheet Model (PISM) – Part 1: Boundary conditions and climatic forcing, The Cryosphere, 14, 599–632, https://doi.org/10.5194/tc-14-599-2020, 2020a.

Albrecht, T., Winkelmann, R., and Levermann, A.: Glacial-cycle simulations of the Antarctic Ice Sheet with the Parallel Ice Sheet Model (PISM) – Part 2: Parameter ensemble analysis, The Cryosphere, 14, 633–656, https://doi.org/10.5194/tc-14-633-2020, 2020b.

Bazin, L., Landais, A., Lemieux-Dudon, B., Toyé Mahamadou Kele, H., Veres, D., Parrenin, F., Martinerie, P., Ritz, C., Capron, E., Lipenkov, V., Loutre, M.-F., Raynaud, D., Vinther, B., Svensson, A., Rasmussen, S. O., Severi, M., Blunier, T., Leuenberger, M., Fischer, H., Masson-Delmotte, V., Chappellaz, J., and Wolff, E.: An optimized multi-proxy, multi-site Antarctic ice and gas orbital chronology (AICC2012): 120-800 ka, Climate of the Past, 9, 1715–1731, https://doi.org/10.5194/cp-9-1715-2013, 2013.

Beem, L., Cavitte, M., Blankenship, D., Carter, S., Young, D., Muldoon, G., Jackson, C., and Siegert, M.: Ice-flow reorganization within the East Antarctic Ice Sheet deep interior, https://doi.org/10.1144/sp461.14, 2018.

Beem, L. H., Young, D. A., Greenbaum, J. S., Blankenship, D. D., Cavitte, M. G. P., Guo, J., and Bo, S.: Aerogeophysical characterization of Titan Dome, East Antarctica, and potential as an ice core target, The Cryosphere, 15, 1719–1730, https://doi.org/10.5194/tc-15-1719-2021, 2021.

Bentley, M. and Wolff, E.: Past interglacial West Antarctic Ice Sheet collapse: a critical review of evidence and approaches, Quaternary Science Reviews, 387, 110 025, https://doi.org/10.1016/j.quascirev.2026.110025, 2026.

Bentley, M. J., Ó Cofaigh, C., Anderson, J. B., Conway, H., Davies, B., Graham, A. G., Hillenbrand, C.-D., Hodgson, D. A., Jamieson, S. S., Larter, R. D., Mackintosh, A., Smith, J. A., Verleyen, E., Ackert, R. P., Bart, P. J., Berg, S., Brunstein, D., Canals, M., Colhoun, E. A., Crosta, X., Dickens, W. A., Domack, E., Dowdeswell, J. A., Dunbar, R., Ehrmann, W., Evans, J., Favier, V., Fink, D., Fogwill, C. J., Glasser, N. F., Gohl, K., Golledge, N. R., Goodwin, I., Gore, D. B., Greenwood, S. L., Hall, B. L., Hall, K., Hedding, D. W., Hein, A. S., Hocking, E. P., Jakobsson, M., Johnson, J. S., Jomelli, V., Jones, R. S., Klages, J. P., Kristoffersen, Y., Kuhn, G., Leventer, A., Licht, K., Lilly, K., Lindow, J., Livingstone, S. J., Massé, G., McGlone, M. S., McKay, R. M., Melles, M., Miura, H., Mulvaney, R., Nel, W., Nitsche, F. O., O'Brien, P. E., Post, A. L., Roberts, S. J., Saunders, K. M., Selkirk, P. M., Simms, A. R., Spiegel, C., Stolldorf, T. D., Sugden, D. E., van der Putten, N., van Ommen, T., Verfaillie, D., Vyverman, W., Wagner, B., White, D. A., Witus, A. E., and Zwartz, D.: A community-based geological reconstruction of Antarctic Ice Sheet deglaciation since the Last Glacial Maximum, Quaternary Science Reviews, 100, 1–9, https://doi.org/10.1016/j.quascirev.2014.06.025, reconstruction of Antarctic Ice Sheet Deglaciation (RAISED), 2014.

Berends, C. J., de Boer, B., and van de Wal, R. S. W.: Reconstructing the evolution of ice sheets, sea level, and atmospheric CO_2 during the past 3.6 million years, Climate of the Past, 17, 361–377, https://doi.org/10.5194/cp-17-361-2021, 2021.

Bernales, J., Rogozhina, I., Greve, R., and Thomas, M.: Comparison of hybrid schemes for the combination of shallow approximations in numerical simulations of the Antarctic Ice Sheet, The Cryosphere, 11, 247–265, https://doi.org/10.5194/tc-11-247-2017, 2017.

Bintanja, R. and Van de Wal, R.: North American ice-sheet dynamics and the onset of 100,000-year glacial cycles, Nature, 454, 869–872, https://doi.org/10.1038/nature07158, 2008.

Bouchet, M., Landais, A., Grisart, A., Parrenin, F., Prié, F., Jacob, R., Fourré, E., Capron, E., Raynaud, D., Lipenkov, V. Y., Loutre, M.-F., Extier, T., Svensson, A., Legrain, E., Martinerie, P., Leuenberger, M., Jiang, W., Ritterbusch, F., Lu, Z.-T., and Yang, G.-M.: The Antarctic Ice Core Chronology 2023 (AICC2023) chronological framework and associated timescale for the European Project for Ice Coring in Antarctica (EPICA) Dome C ice core, Climate of the Past, 19, 2257–2286, https://doi.org/10.5194/cp-19-2257-2023, 2023.

https://doi.org/10.5194/egusphere-2026-5136
Preprint. Discussion started: 31 August 2026

Briggs, R. D. and Tarasov, L.: How to evaluate model-derived deglaciation chronologies: a case study using Antarctica, Quaternary Science Reviews, 63, 109–127, https://doi.org/10.1016/j.quascirev.2012.11.021, 2013.

Briggs, R. D., Pollard, D., and Tarasov, L.: A data-constrained large ensemble analysis of Antarctic evolution since the Eemian, Quaternary Science Reviews, 103, 91–115, https://doi.org/10.1016/j.quascirev.2014.09.003, 2014.

Budd, W. and Jenssen, D.: Numerical modelling of the large-scale basal water flux under the West Antarctic Ice Sheet, in: Dynamics of the West Antarctic Ice Sheet: Proceedings of a Workshop held in Utrecht, May 6–8, 1985, pp. 293–320, Springer, https://doi.org/10.1007/978-94-009-3745-1_16, 1987.

Budd, W. F., Keage, P. L., and Blundy, N. A.: Empirical Studies of Ice Sliding, Journal of Glaciology, 23, 157–170, https://doi.org/10.3189/S0022143000029804, 1979.

Bueler, E. and Brown, J.: Shallow shelf approximation as a "sliding law" in a thermomechanically coupled ice sheet model, Journal of Geophysical Research: Earth Surface, 114, F03 008, https://doi.org/10.1029/2008JF001179, 2009.

Buizert, C., Fudge, T. J., Roberts, W. H. G., Steig, E. J., Sherriff-Tadano, S., Ritz, C., Lefebvre, E., Edwards, J., Kawamura, K., Oyabu, I., Motoyama, H., Kahle, E. C., Jones, T. R., Abe-Ouchi, A., Obase, T., Martin, C., Corr, H., Severinghaus, J. P., Beaudette, R., Epifanio, J. A., Brook, E. J., Martin, K., Chappellaz, J., Aoki, S., Nakazawa, T., Sowers, T. A., Alley, R. B., Ahn, J., Sigl, M., Severi, M., Dunbar, N. W., Svensson, A., Fegyveresi, J. M., He, C., Liu, Z., Zhu, J., Otto-Bliesner, B. L., Lipenkov, V. Y., Kageyama, M., and Schwander, J.: Antarctic surface temperature and elevation during the Last Glacial Maximum, Science, 372, 1097–1101, https://doi.org/10.1126/science.abd2897, 2021.

Burton-Johnson, A., Dziadek, R., and Martin, C.: Review article: Geothermal heat flow in Antarctica: current and future directions, The Cryosphere, 14, 3843–3873, https://doi.org/10.5194/tc-14-3843-2020, 2020.

Calov, R. and Greve, R.: A semi-analytical solution for the positive degree-day model with stochastic temperature variations, Journal of Glaciology, 51, 173–175, https://doi.org/10.3189/172756505781829601, 2005.

Carson, C. J., McLaren, S., Roberts, J. L., Boger, S. D., and Blankenship, D. D.: Hot rocks in a cold place: high sub-glacial heat flow in East Antarctica, Journal of the Geological Society, 171, 9–12, https://doi.org/10.1144/jgs2013-030, 2013.

Chandler, D. M., Langebroek, P. M., Reese, R., Albrecht, T., Garbe, J., and Winkelmann, R.: Antarctic Ice Sheet tipping in the last 800,000 years warns of future ice loss, Communications Earth & Environment, 6, 420, https://doi.org/10.1038/s43247-025-02366-2, 2025.

Chen, B., Haeger, C., Kaban, M. K., and Petrunin, A. G.: Variations of the effective elastic thickness reveal tectonic fragmentation of the Antarctic lithosphere, Tectonophysics, 746, 412–424, https://doi.org/https://doi.org/10.1016/j.tecto.2017.06.012, understanding geological processes through modelling - A Memorial Volume honouring Evgenii Burov, 2018.

Chung, A., Parrenin, F., Steinhage, D., Mulvaney, R., Martín, C., Cavitte, M. G. P., Lilien, D. A., Helm, V., Taylor, D., Gogineni, P., Ritz, C., Frezzotti, M., O'Neill, C., Miller, H., Dahl-Jensen, D., and Eisen, O.: Stagnant ice and age modelling in the Dome C region, Antarctica, The Cryosphere, 17, 3461–3483, https://doi.org/10.5194/tc-17-3461-2023, 2023.

Chung, A., Parrenin, F., Mulvaney, R., Vittuari, L., Frezzotti, M., Zanutta, A., Lilien, D. A., Cavitte, M. G. P., and Eisen, O.: Age, thinning and spatial origin of the Beyond EPICA ice from a 2.5D ice flow model, The Cryosphere, 19, 4125–4140, https://doi.org/10.5194/tc-19-4125-2025, 2025.

Coulon, V., Bulthuis, K., Whitehouse, P. L., Sun, S., Haubner, K., Zipf, L., and Pattyn, F.: Contrasting Response of West and East Antarctic Ice Sheets to Glacial Isostatic Adjustment, Journal of Geophysical Research: Earth Surface, 126, e2020JF006 003, https://doi.org/10.1029/2020JF006003, e2020JF006003 2020JF006003, 2021.

Coulon, V., Klose, A. K., Kittel, C., Edwards, T., Turner, F., Winkelmann, R., and Pattyn, F.: Disentangling the drivers of future Antarctic ice loss with a historically calibrated ice-sheet model, The Cryosphere, 18, 653–681, https://doi.org/10.5194/tc-18-653-2024, 2024.

Coulon, V., Klose, A. K., Edwards, T., Turner, F., Pattyn, F., and Winkelmann, R.: From short-term uncertainties to long-term certainties in the future evolution of the Antarctic Ice Sheet, Nature communications, 16, 10 385, https://doi.org/10.1038/s41467-025-66178-w, 2025.

Dawson, E. J., Schroeder, D. M., Chu, W., Mantelli, E., and Seroussi, H.: Ice mass loss sensitivity to the Antarctic ice sheet basal thermal state, Nature Communications, 13, 4957, https://doi.org/10.1038/s41467-022-32632-2, 2022.

DeConto, R. M. and Pollard, D.: Contribution of Antarctica to past and future sea-level rise, Nature, 531, 591–597, https://doi.org/10.1038/nature17145, 2016.

Ekaykin, A., Lipenkov, V. Y., and Tchikhatchev, K.: Preservation of the Climatic Signal in the Old Ice Layers at the Dome B Area (Antarctica), Izvestiya, Atmospheric and Oceanic Physics, 59, S1–S7, https://doi.org/10.1134/S0001433823130066, 2023.

Ekaykin, A. A., Bolshunov, A. V., Lipenkov, V. Y., Scheinert, M., Eberlein, L., Brovkov, E., Popov, S. V., and Turkeev, A. V.: First glaciological investigations at Ridge B, central East Antarctica, Antarctic Science, 33, 418–427, https://doi.org/10.1017/S0954102021000171, 2021.

Fischer, H., Severinghaus, J., Brook, E., Wolff, E., Albert, M., Alemany, O., Arthern, R., Bentley, C., Blankenship, D., Chappellaz, J., Creyts, T., Dahl-Jensen, D., Dinn, M., Frezzotti, M., Fujita, S., Gallee, H., Hindmarsh, R., Hudspeth, D., Jugie, G., Kawamura, K., Lipenkov, V., Miller, H., Mulvaney, R., Parrenin, F., Pattyn, F., Ritz, C., Schwander, J., Steinhage, D., van Ommen, T., and Wilhelms, F.: Where to find 1.5 million yr old ice for the IPICS "Oldest-Ice" ice core, Climate of the Past, 9, 2489–2505, https://doi.org/10.5194/cp-9-2489-2013, 2013.

Frieler, K., Clark, P. U., He, F., Buizert, C., Reese, R., Ligtenberg, S. R., Van Den Broeke, M. R., Winkelmann, R., and Levermann, A.: Consistent evidence of increasing Antarctic accumulation with warming, Nature Climate Change, 5, 348–352, https://doi.org/10.1038/nclimate2574, 2015.

Fudge, T. J., Hills, B. H., Horlings, A. N., Holschuh, N., Christian, J. E., Davidge, L., Hoffman, A., O'Connor, G. K., Christianson, K., and Steig, E. J.: A site for deep ice coring at West Hercules Dome: results from ground-based geophysics and modeling, Journal of Glaciology, 69, 538–550, https://doi.org/10.1017/jog.2022.80, 2023.

Gillet-Chaulet, F. and Hindmarsh, R. C. A.: Flow at ice-divide triple junctions: 1. Three-dimensional full-Stokes modeling, Journal of Geophysical Research: Earth Surface, 116, https://doi.org/10.1029/2009JF001611, 2011.

Girden, E. R.: ANOVA: Repeated measures, 84, sage, 1992.

Golledge, N. R., Kowalewski, D. E., Naish, T. R., Levy, R. H., Fogwill, C. J., and Gasson, E. G.: The multi-millennial Antarctic commitment to future sea-level rise, Nature, 526, 421–425, https://doi.org/10.1038/nature15706, 2015.

Goosse, H., Crespin, E., de Montety, A., Mann, M. E., Renssen, H., and Timmermann, A.: Reconstructing surface temperature changes over the past 600 years using climate model simulations with data assimilation, Journal of Geophysical Research: Atmospheres, 115, https://doi.org/10.1029/2009JD012737, 2010.

Haeger, C., Petrunin, A. G., and Kaban, M. K.: Geothermal Heat Flow and Thermal Structure of the Antarctic Lithosphere, Geochemistry, Geophysics, Geosystems, 23, e2022GC010 501, https://doi.org/10.1029/2022GC010501, 2022.

Hajima, T., Abe, M., Arakawa, O., Suzuki, T., Komuro, Y., Ogura, T., Ogochi, K., Watanabe, M., Yamamoto, A., Tatebe, H., Noguchi, M. A., Ohgaito, R., Ito, A., Yamazaki, D., Ito, A., Takata, K., Watanabe, S., Kawamiya, M., and Tachiiri, K.: MIROC MIROC-ES2L model output prepared for CMIP6 CMIP historical, https://doi.org/10.22033/ESGF/CMIP6.5602, 2019.

https://doi.org/10.5194/egusphere-2026-5136
Preprint. Discussion started: 31 August 2026

Hills, B. H., Holschuh, N., Hoffman, A. O., Horlings, A. N., Erwin, E., Kirkpatrick, L. R., Fudge, T. J., Steig, E. J., and Christianson, K.: Radar-Derived Crystal Orientation Fabric Suggests Dynamic Stability at the Summit of Hercules Dome, Journal of Geophysical Research: Earth Surface, 130, e2023JF007 588, https://doi.org/10.1029/2023JF007588, e2023JF007588 2023JF007588, 2025.

Hindmarsh, R. C.: On the numerical computation of temperature in an ice sheet, Journal of Glaciology, 45, 568–574, https://doi.org/10.3189/S0022143000001441, 1999.

Hindmarsh, R. C., Gwendolyn, J.-M., and Parrenin, F.: A large-scale numerical model for computing isochrone geometry, Annals of Glaciology, 50, 130–140, https://doi.org/10.3189/172756409789097450, 2009.

Hindmarsh, R. G. A.: Stochastic perturbation of divide position, Annals of Glaciology, 23, 94–104, https://doi.org/10.3189/S0260305500013306, 1996.

Huybrechts, P.: The Antarctic ice sheet and environmental change: a three-dimensional modelling study, PhD thesis, Vrije Universiteit of Brussel, available at: https://hdl.handle.net/10013/epic.12054, 1992.

Huybrechts, P.: Report of the Third EISMINT Workshop on Model Intercomparison, http://hdl.handle.net/10013/epic.17327.d001, 1998.

Jacobel, R. W., Welch, B. C., Steig, E. J., and Schneider, D. P.: Glaciological and climatic significance of Hercules Dome, Antarctica: An optimal site for deep ice core drilling, Journal of Geophysical Research: Earth Surface, 110, https://doi.org/10.1029/2004JF000188, 2005.

Jordan, T., Martin, C., Ferraccioli, F., Matsuoka, K., Corr, H., Forsberg, R., Olesen, A., and Siegert, M.: Anomalously high geothermal flux near the South Pole, Scientific reports, 8, 16 785, https://doi.org/10.1038/s41598-018-35182-0, 2018.

Jouzel, J., Masson-Delmotte, V., Cattani, O., Dreyfus, G., Falourd, S., Hoffmann, G., Minster, B., Nouet, J., Barnola, J. M., Chappellaz, J., Fischer, H., Gallet, J. C., Johnsen, S., Leuenberger, M., Loulergue, L., Luethi, D., Oerter, H., Parrenin, F., Raisbeck, G., Raynaud, D., Schilt, A., Schwander, J., Selmo, E., Souchez, R., Spahni, R., Stauffer, B., Steffensen, J. P., Stenni, B., Stocker, T. F., Tison, J. L., Werner, M., and Wolff, E. W.: Orbital and Millennial Antarctic Climate Variability over the Past 800,000 Years, Science, 317, 793–796, https://doi.org/10.1126/science.1141038, 2007.

Karlsson, N. B., Binder, T., Eagles, G., Helm, V., Pattyn, F., Van Liefferinge, B., and Eisen, O.: Glaciological characteristics in the Dome Fuji region and new assessment for "Oldest Ice", The Cryosphere, 12, 2413–2424, https://doi.org/10.5194/tc-12-2413-2018, 2018.

Kawamura, K., Abe-Ouchi, A., Motoyama, H., Ageta, Y., Aoki, S., Azuma, N., Fujii, Y., Fujita, K., Fujita, S., Fukui, K., Furukawa, T., Furusaki, A., Goto-Azuma, K., Greve, R., Hirabayashi, M., Hondoh, T., Hori, A., Horikawa, S., Horiuchi, K., Igarashi, M., Iizuka, Y., Kameda, T., Kanda, H., Kohno, M., Kuramoto, T., Matsushi, Y., Miyahara, M., Miyake, T., Miyamoto, A., Nagashima, Y., Nakayama, Y., Nakazawa, T., Nakazawa, F., Nishio, F., Obinata, I., Ohgaito, R., Oka, A., Okuno, J., Okuyama, J., Oyabu, I., Parrenin, F., Pattyn, F., Saito, F., Saito, T., Saito, T., Sakurai, T., Sasa, K., Seddik, H., Shibata, Y., Shinbori, K., Suzuki, K., Suzuki, T., Takahashi, A., Takahashi, K., Takahashi, S., Takata, M., Tanaka, Y., Uemura, R., Watanabe, G., Watanabe, O., Yamasaki, T., Yokoyama, K., Yoshimori, M., and Yoshimoto, T.: State dependence of climatic instability over the past 720,000 years from Antarctic ice cores and climate modeling, Science Advances, 3, e1600 446, https://doi.org/10.1126/sciadv.1600446, 2017.

Kerr, M., Young, D. A., Yan, S., and Pierce, C.: Radar Specularity Content Indicates a Strong Geothermal Heat Flow Gradient in Antarctica's South Pole Basin, Geophysical Research Letters, 53, e2025GL120 928, https://doi.org/10.1029/2025GL120928, e2025GL120928 2025GL120928, 2026.

Kittel, C., Amory, C., Agosta, C., Jourdain, N. C., Hofer, S., Delhasse, A., Doutreloup, S., Huot, P.-V., Lang, C., Fichefet, T., and Fettweis, X.: Diverging future surface mass balance between the Antarctic ice shelves and grounded ice sheet, The Cryosphere, 15, 1215–1236, https://doi.org/10.5194/tc-15-1215-2021, 2021.

Klose, A. K., Coulon, V., Pattyn, F., and Winkelmann, R.: The long-term sea-level commitment from Antarctica, The Cryosphere, 18, 4463–4492, https://doi.org/10.5194/tc-18-4463-2024, 2024.

Koutnik, M. R., Fudge, T. J., Conway, H., Waddington, E. D., Neumann, T. A., Cuffey, K. M., Buizert, C., and Taylor, K. C.: Holocene accumulation and ice flow near the West Antarctic Ice Sheet Divide ice core site, Journal of Geophysical Research: Earth Surface, 121, 907–924, https://doi.org/10.1002/2015JF003668, 2016.

Kreuzer, M., Reese, R., Huiskamp, W. N., Petri, S., Albrecht, T., Feulner, G., and Winkelmann, R.: Coupling framework (1.0) for the PISM (1.1.4) ice sheet model and the MOM5 (5.1.0) ocean model via the PICO ice shelf cavity model in an Antarctic domain, Geoscientific Model Development, 14, 3697–3714, https://doi.org/10.5194/gmd-14-3697-2021, 2021.

Lang, S., Yang, M., Cui, X., Li, L., Wang, X., Guo, J., Greenbaum, J. S., Sun, B., and Siegert, M. J.: Geothermal heat flux of Ridge B region in Antarctica inferred from basal dry–wet distribution, Journal of Glaciology, 71, e12, https://doi.org/10.1017/jog.2024.85, 2025.

Lecavalier, B., Tarasov, L., Balco, G., Spector, P., Hillenbrand, C.-D., Buizert, C., Ritz, C., Leduc-Leballeur, M., Mulvaney, R., Whitehouse, P. L., Bentley, M. J., and Bamber, J.: Antarctic ice sheet paleo-constraint database., https://theghub.org/resources/4884, available at: https://theghub.org/resources/4884, 2022.

Lecavalier, B. S. and Tarasov, L.: A history-matching analysis of the Antarctic Ice Sheet since the Last Interglacial – Part 1: Ice sheet evolution, The Cryosphere, 19, 919–953, https://doi.org/10.5194/tc-19-919-2025, 2025.

Lecavalier, B. S., Tarasov, L., Balco, G., Spector, P., Hillenbrand, C.-D., Buizert, C., Ritz, C., Leduc-Leballeur, M., Mulvaney, R., Whitehouse, P. L., Bentley, M. J., and Bamber, J.: Antarctic Ice Sheet paleo-constraint database, Earth System Science Data, 15, 3573–3596, https://doi.org/10.5194/essd-15-3573-2023, 2023.

Leysinger Vieli, G. J.-M. C., Siegert, M. J., and Payne, A. J.: Reconstructing ice-sheet accumulation rates at ridge B, East Antarctica, Annals of Glaciology, 39, 326–330, https://doi.org/10.3189/172756404781814519, 2004.

Leysinger Vieli, G. J.-M. C., Hindmarsh, R. C. A., Siegert, M. J., and Bo, S.: Time-dependence of the spatial pattern of accumulation rate in East Antarctica deduced from isochronic radar layers using a 3-D numerical ice flow model, Journal of Geophysical Research: Earth Surface, 116, https://doi.org/10.1029/2010JF001785, 2011.

Leysinger Vieli, G.-M., Martin, C., Hindmarsh, R., and Lüthi, M. P.: Basal freeze-on generates complex ice-sheet stratigraphy, Nature communications, 9, 4669, https://doi.org/10.1038/s41467-018-07083-3, 2018.

Li, D., Tang, X., Chung, A., Parrenin, F., and Sun, B.: Simulated evidence for ice over 1 Ma in the Dome A region, East Antarctica, EGUsphere, 2026, 1–18, https://doi.org/10.5194/egusphere-2025-5165, 2026.

Lilien, D. A., Steinhage, D., Taylor, D., Parrenin, F., Ritz, C., Mulvaney, R., Martín, C., Yan, J.-B., O'Neill, C., Frezzotti, M., Miller, H., Gogineni, P., Dahl-Jensen, D., and Eisen, O.: Brief communication: New radar constraints support presence of ice older than 1.5 Myr at Little Dome C, The Cryosphere, 15, 1881–1888, https://doi.org/10.5194/tc-15-1881-2021, 2021.

Lisiecki, L. E. and Raymo, M. E.: A Pliocene-Pleistocene stack of 57 globally distributed benthic δ18O records, Paleoceanography, 20, https://doi.org/10.1029/2004PA001071, 2005.

Livingstone, S. J., Li, Y., Rutishauser, A., Sanderson, R. J., Winter, K., Mikucki, J. A., Björnsson, H., Bowling, J. S., Chu, W., Dow, C. F., et al.: Subglacial lakes and their changing role in a warming climate, Nature Reviews Earth & Environment, 3, 106–124, https://doi.org/10.1038/s43017-021-00246-9, 2022.

Lliboutry, L.: A critical review of analytical approximate solutions for steady state velocities and temperatures in cold ice-sheets, Gletscherkd. Glazialgeol., 15, 135–148, https://cir.nii.ac.jp/crid/1370857593652763175, URL: https://cir.nii.ac.jp/crid/1370857593652763175, 1979.

https://doi.org/10.5194/egusphere-2026-5136
Preprint. Discussion started: 31 August 2026

Lösing, M. and Ebbing, J.: Predicting Geothermal Heat Flow in Antarctica With a Machine Learning Approach, Journal of Geophysical Research: Solid Earth, 126, e2020JB021 499, https://doi.org/10.1029/2020JB021499, 2021.

Lösing, M., Colgan, W., Stål, T., Ebbing, J., Busck, A. G., Zhang, T., Seroussi, H. L., McCormack, F., Fahrner, D., Stearns, L., Svendsen, S. H., and Reading, A.: Community heat flow recommendations: suitable basal boundary conditions for Greenland and Antarctica in ISMIP7, GEUS Bulletin, 62, https://doi.org/10.34194/r0w9rf81, 2026.

Maris, M. N. A., de Boer, B., Ligtenberg, S. R. M., Crucifix, M., van de Berg, W. J., and Oerlemans, J.: Modelling the evolution of the Antarctic ice sheet since the last interglacial, The Cryosphere, 8, 1347–1360, https://doi.org/10.5194/tc-8-1347-2014, 2014.

Martos, Y. M., Catalán, M., Jordan, T. A., Golynsky, A., Golynsky, D., Eagles, G., and Vaughan, D. G.: Heat Flux Distribution of Antarctica Unveiled, Geophysical Research Letters, 44, 11 417–11 426, https://doi.org/10.1002/2017GL075609, 2017.

Martín, C., Hindmarsh, R. C. A., and Navarro, F. J.: On the effects of divide migration, along-ridge flow, and basal sliding on isochrones near an ice divide, Journal of Geophysical Research: Earth Surface, 114, https://doi.org/10.1029/2008JF001025, 2009.

Morlighem, M.: MEaSUREs BedMachine Antarctica, Version 3, https://doi.org/10.5067/FPSU0V1MWUB6, 2022.

Morlighem, M., Rignot, E., Binder, T., Blankenship, D., Drews, R., Eagles, G., Eisen, O., Ferraccioli, F., Forsberg, R., Fretwell, P., et al.: Deep glacial troughs and stabilizing ridges unveiled beneath the margins of the Antarctic ice sheet, Nature geoscience, 13, 132–137, https://doi.org/10.1038/s41561-019-0510-8, 2020.

Mouginot, J., Rignot, E., and Scheuchl, B.: Continent-Wide, Interferometric SAR Phase, Mapping of Antarctic Ice Velocity, Geophysical Research Letters, 46, 9710–9718, https://doi.org/10.1029/2019GL083826, 2019a.

Mouginot, J., Rignot, E., and Scheuchl, B.: MEaSUREs Phase-Based Antarctica Ice Velocity Map, Version 1, https://doi.org/10.5067/PZ3NJ5RXRH10, 2019b.

Nereson, N. A. and Waddington, E. D.: Isochrones and isotherms beneath migrating ice divides, Journal of Glaciology, 48, 95–108, https://doi.org/10.3189/172756502781831647, 2002.

Nereson, N. A., Raymond, C. F., Waddington, E. D., and Jacobel, R. W.: Migration of the Siple Dome ice divide, West Antarctica, Journal of Glaciology, 44, 643–652, https://doi.org/10.3189/S0022143000002148, 1998.

Obase, T., Abe-Ouchi, A., Saito, F., Tsutaki, S., Fujita, S., Kawamura, K., and Motoyama, H.: A one-dimensional temperature and age modeling study for selecting the drill site of the oldest ice core near Dome Fuji, Antarctica, The Cryosphere, 17, 2543–2562, https://doi.org/10.5194/tc-17-2543-2023, 2023.

Ohgaito, R., Abe-Ouchi, A., Abe, M., Arakawa, O., Ogochi, K., Hajima, T., Watanabe, M., Yamamoto, A., Tatebe, H., Noguchi, M. A., Ito, A., Yamazaki, D., Ito, A., Takata, K., Watanabe, S., Kawamiya, M., and Tachiiri, K.: MIROC MIROC-ES2L model output prepared for CMIP6 PMIP lgm, https://doi.org/10.22033/ESGF/CMIP6.5644, 2019.

Ohgaito, R., Yamamoto, A., Hajima, T., O'ishi, R., Abe, M., Tatebe, H., Abe-Ouchi, A., and Kawamiya, M.: PMIP4 experiments using MIROC-ES2L Earth system model, Geoscientific Model Development, 14, 1195–1217, https://doi.org/10.5194/gmd-14-1195-2021, 2021.

O'ishi, R., Abe-Ouchi, A., Ohgaito, R., Abe, M., Arakawa, O., Ogochi, K., Hajima, T., Watanabe, M., Yamamoto, A., Tatebe, H., Noguchi, M. A., Ito, A., Yamazaki, D., Ito, A., Takata, K., Watanabe, S., Kawamiya, M., and Tachiiri, K.: MIROC MIROC-ES2L model output prepared for CMIP6 PMIP lig127k, https://doi.org/10.22033/ESGF/CMIP6.5645, 2019.

Park, I.-W., Jin, E. K., Morlighem, M., and Lee, K.-K.: Impact of boundary conditions on the modeled thermal regime of the Antarctic ice sheet, The Cryosphere, 18, 1139–1155, https://doi.org/10.5194/tc-18-1139-2024, 2024.

Parrenin, F., Rémy, F., Ritz, C., Siegert, M. J., and Jouzel, J.: New modeling of the Vostok ice flow line and implication for the glaciological chronology of the Vostok ice core, Journal of Geophysical Research: Atmospheres, 109, https://doi.org/10.1029/2004JD004561, 2004.

https://doi.org/10.5194/egusphere-2026-5136
Preprint. Discussion started: 31 August 2026

Parrenin, F., Dreyfus, G., Durand, G., Fujita, S., Gagliardini, O., Gillet, F., Jouzel, J., Kawamura, K., Lhomme, N., Masson-Delmotte, V., Ritz, C., Schwander, J., Shoji, H., Uemura, R., Watanabe, O., and Yoshida, N.: 1-D-ice flow modelling at EPICA Dome C and Dome Fuji, East Antarctica, Climate of the Past, 3, 243–259, https://doi.org/10.5194/cp-3-243-2007, 2007.

Parrenin, F., Cavitte, M. G. P., Blankenship, D. D., Chappellaz, J., Fischer, H., Gagliardini, O., Masson-Delmotte, V., Passalacqua, O., Ritz, C., Roberts, J., Siegert, M. J., and Young, D. A.: Is there 1.5-million-year-old ice near Dome C, Antarctica?, The Cryosphere, 11, 2427–2437, https://doi.org/10.5194/tc-11-2427-2017, 2017.

Passalacqua, O., Gagliardini, O., Parrenin, F., Todd, J., Gillet-Chaulet, F., and Ritz, C.: Performance and applicability of a 2.5-D ice-flow model in the vicinity of a dome, Geoscientific Model Development, 9, 2301–2313, https://doi.org/10.5194/gmd-9-2301-2016, 2016.

Passalacqua, O., Ritz, C., Parrenin, F., Urbini, S., and Frezzotti, M.: Geothermal flux and basal melt rate in the Dome C region inferred from radar reflectivity and heat modelling, The Cryosphere, 11, 2231–2246, https://doi.org/10.5194/tc-11-2231-2017, 2017.

Pattyn, F.: Sea-level response to melting of Antarctic ice shelves on multi-centennial timescales with the fast Elementary Thermomechanical Ice Sheet model (f.ETISh v1. 0), The Cryosphere, 11, 1851–1878, https://doi.org/10.5194/tc-11-1851-2017, 2017.

Petit, J.-R., Jouzel, J., Raynaud, D., Barkov, N. I., Barnola, J.-M., Basile, I., Bender, M., Chappellaz, J., Davis, M., Delaygue, G., et al.: Climate and atmospheric history of the past 420,000 years from the Vostok ice core, Antarctica, Nature, 399, 429–436, https://doi.org/10.1038/20859, 1999.

Pollard, D. and DeConto, R. M.: Description of a hybrid ice sheet-shelf model, and application to Antarctica, Geoscientific Model Development, 5, 1273–1295, https://doi.org/10.5194/gmd-5-1273-2012, 2012a.

Pollard, D. and DeConto, R. M.: A simple inverse method for the distribution of basal sliding coefficients under ice sheets, applied to Antarctica, The Cryosphere, 6, 953–971, https://doi.org/10.5194/tc-6-953-2012, 2012b.

Pollard, D. and DeConto, R. M.: Improvements in one-dimensional grounding-line parameterizations in an ice-sheet model with lateral variations (PSUICE3D v2.1), Geoscientific Model Development, 13, 6481–6500, https://doi.org/10.5194/gmd-13-6481-2020, 2020.

Pollard, D., DeConto, R. M., and Alley, R. B.: Potential Antarctic Ice Sheet retreat driven by hydrofracturing and ice cliff failure, Earth and Planetary Science Letters, 412, 112–121, https://doi.org/10.1016/j.epsl.2014.12.035, 2015.

Pollard, D., Chang, W., Haran, M., Applegate, P., and DeConto, R.: Large ensemble modeling of the last deglacial retreat of the West Antarctic Ice Sheet: comparison of simple and advanced statistical techniques, Geoscientific Model Development, 9, 1697–1723, https://doi.org/10.5194/gmd-9-1697-2016, 2016.

Price, S. F., Conway, H., and Waddington, E. D.: Evidence for late Pleistocene thinning of Siple Dome, West Antarctica, Journal of Geophysical Research: Earth Surface, 112, https://doi.org/10.1029/2006JF000725, 2007.

Quiquet, A., Dumas, C., Ritz, C., Peyaud, V., and Roche, D. M.: The GRISLI ice sheet model (version 2.0): calibration and validation for multi-millennial changes of the Antarctic ice sheet, Geoscientific Model Development, 11, 5003–5025, https://doi.org/10.5194/gmd-11-5003-2018, 2018.

Raspoet, O. and Pattyn, F.: Estimates of basal and englacial thermal conditions of the Antarctic ice sheet, Journal of Glaciology, 71, e104, https://doi.org/10.1017/jog.2025.10087, 2025a.

Raspoet, O. and Pattyn, F.: Estimates of basal and englacial thermal conditions of the Antarctic ice sheet, https://doi.org/10.5281/zenodo.15664172, 2025b.

Raspoet, O., Coulon, V., and Pattyn, F.: Stability and basal thermal conditions of East Antarctic divide regions during the last glacial cycle, https://doi.org/10.5281/zenodo.22047133, 2026.

Raymond, C. F.: Deformation in the Vicinity of Ice Divides, Journal of Glaciology, 29, 357–373, https://doi.org/10.3189/S0022143000030288, 1983.

Reading, A. M., Stål, T., Halpin, J. A., Lösing, M., Ebbing, J., Shen, W., McCormack, F. S., Siddoway, C. S., and Hasterok, D.: Antarctic geothermal heat flow and its implications for tectonics and ice sheets, Nature Reviews Earth & Environment, 3, 814–831, https://doi.org/10.1038/s43017-022-00348-y, 2022.

Reeh, N.: Parameterization of melt rate and surface temperature on the Greenland ice sheet, Polarforschung, 59, 113–128, 1991.

Reese, R., Albrecht, T., Mengel, M., Asay-Davis, X., and Winkelmann, R.: Antarctic sub-shelf melt rates via PICO, The Cryosphere, 12, 1969–1985, https://doi.org/10.5194/tc-12-1969-2018, 2018.

Ritz, C.: Time dependent boundary conditions for calculation of temperature fields in ice sheets, IAHS Publication, 170, 207–216, URL: https://cir.nii.ac.jp/crid/1370002216709300101, 1987.

Ritz, C.: Un modèle thermo-mécanique d'évolution pour le bassin glaciaire Antarctique Vostok-Glacier Byrd : Sensibilité aux valeurs des paramètres mal connus., Theses, Université Joseph-Fourier - Grenoble I, https://theses.hal.science/tel-00693923, available at: https://theses.hal.science/tel-00693923, 1992.

Ritz, C., Rommelaere, V., and Dumas, C.: Modeling the evolution of Antarctic ice sheet over the last 420,000 years: Implications for altitude changes in the Vostok region, Journal of Geophysical Research: Atmospheres, 106, 31 943–31 964, https://doi.org/10.1029/2001JD900232, 2001.

Sanderson, R. J., Ross, N., Winter, K., Bingham, R. G., Callard, S. L., Jordan, T. A., and Young, D. A.: Dated radar-stratigraphy between Dome A and South Pole, East Antarctica: old ice potential and ice sheet history, Journal of Glaciology, 70, e74, https://doi.org/10.1017/jog.2024.60, 2024.

Schmidtko, S., Heywood, K. J., Thompson, A. F., and Aoki, S.: Multidecadal warming of Antarctic waters, Science, 346, 1227–1231, https://doi.org/10.1126/science.1256117, 2014.

Schoof, C.: Ice sheet grounding line dynamics: Steady states, stability, and hysteresis, Journal of Geophysical Research: Earth Surface, 112, https://doi.org/10.1029/2006JF000664, 2007.

Seiner, O., Hugney, A., Seroussi, H., and MacGregor, J. A.: A synthesis of the basal thermal state of the Antarctic ice sheet, Journal of Glaciology, 71, e127, https://doi.org/10.1017/jog.2025.10102, 2025.

Seroussi, H., Pelle, T., Lipscomb, W. H., Abe-Ouchi, A., Albrecht, T., Alvarez-Solas, J., Asay-Davis, X., Barre, J.-B., Berends, C. J., Bernales, J., Blasco, J., Caillet, J., Chandler, D. M., Coulon, V., Cullather, R., Dumas, C., Galton-Fenzi, B. K., Garbe, J., Gillet-Chaulet, F., Gladstone, R., Goelzer, H., Golledge, N., Greve, R., Gudmundsson, G. H., Han, H. K., Hillebrand, T. R., Hoffman, M. J., Huybrechts, P., Jourdain, N. C., Klose, A. K., Langebroek, P. M., Leguy, G. R., Lowry, D. P., Mathiot, P., Montoya, M., Morlighem, M., Nowicki, S., Pattyn, F., Payne, A. J., Quiquet, A., Reese, R., Robinson, A., Saraste, L., Simon, E. G., Sun, S., Twarog, J. P., Trusel, L. D., Urruty, B., Van Breedam, J., van de Wal, R. S. W., Wang, Y., Zhao, C., and Zwinger, T.: Evolution of the Antarctic Ice Sheet Over the Next Three Centuries From an ISMIP6 Model Ensemble, Earth's Future, 12, e2024EF004 561, https://doi.org/https://doi.org/10.1029/2024EF004561, e2024EF004561 2024EF004561, 2024.

Shen, W., Wiens, D. A., Lloyd, A. J., and Nyblade, A. A.: A Geothermal Heat Flux Map of Antarctica Empirically Constrained by Seismic Structure, Geophysical Research Letters, 47, e2020GL086 955, https://doi.org/10.1029/2020GL086955, 2020.

Siegert, M. J., Eyers, R. D., and Tabacco, I. E.: Three-dimensional ice sheet structure at Dome C, central East Antarctica: implications for the interpretation of the EPICA ice core, Antarctic Science, 13, 182–187, https://doi.org/10.1017/S095410200100027X, 2001.

Snyder, C. W.: Evolution of global temperature over the past two million years, Nature, 538, 226–228, https://doi.org/10.1038/nature19798, 2016.

Spratt, R. M. and Lisiecki, L. E.: A Late Pleistocene sea level stack, Climate of the Past, 12, 1079–1092, https://doi.org/10.5194/cp-12-1079-2016, 2016.

Steinhage, D., Kipfstuhl, S., Nixdorf, U., and Miller, H.: Internal structure of the ice sheet between Kohnen station and Dome Fuji, Antarctica, revealed by airborne radio-echo sounding, Annals of Glaciology, 54, 163–167, https://doi.org/10.3189/2013AoG64A113, 2013.

Stål, T., Reading, A. M., Halpin, J. A., and Whittaker, J. M.: Antarctic Geothermal Heat Flow Model: Aq1, Geochemistry, Geophysics, Geosystems, 22, e2020GC009 428, https://doi.org/10.1029/2020GC009428, 2021.

Sun, B., Moore, J. C., Zwinger, T., Zhao, L., Steinhage, D., Tang, X., Zhang, D., Cui, X., and Martín, C.: How old is the ice beneath Dome A, Antarctica?, The Cryosphere, 8, 1121–1128, https://doi.org/10.5194/tc-8-1121-2014, 2014.

Sutter, J., Gierz, P., Grosfeld, K., Thoma, M., and Lohmann, G.: Ocean temperature thresholds for Last Interglacial West Antarctic Ice Sheet collapse, Geophysical Research Letters, 43, 2675–2682, https://doi.org/10.1002/2016GL067818, 2016.

Sutter, J., Fischer, H., Grosfeld, K., Karlsson, N. B., Kleiner, T., Van Liefferinge, B., and Eisen, O.: Modelling the Antarctic Ice Sheet across the mid-Pleistocene transition – implications for Oldest Ice, The Cryosphere, 13, 2023–2041, https://doi.org/10.5194/tc-13-2023-2019, 2019.

Talalay, P., Li, Y., Augustin, L., Clow, G. D., Hong, J., Lefebvre, E., Markov, A., Motoyama, H., and Ritz, C.: Geothermal heat flux from measured temperature profiles in deep ice boreholes in Antarctica, The Cryosphere, 14, 4021–4037, https://doi.org/10.5194/tc-14-4021-2020, 2020.

Uemura, R., Motoyama, H., Masson-Delmotte, V., Jouzel, J., Kawamura, K., Goto-Azuma, K., Fujita, S., Kuramoto, T., Hirabayashi, M., Miyake, T., et al.: Asynchrony between Antarctic temperature and CO2 associated with obliquity over the past 720,000 years, Nature communications, 9, 961, https://doi.org/10.1038/s41467-018-03328-3, 2018.

Urbini, S., Frezzotti, M., Gandolfi, S., Vincent, C., Scarchilli, C., Vittuari, L., and Fily, M.: Historical behaviour of Dome C and Talos Dome (East Antarctica) as investigated by snow accumulation and ice velocity measurements, Global and Planetary Change, 60, 576–588, https://doi.org/10.1016/j.gloplacha.2007.08.002, 2008.

van Aalderen, V. M., Quiquet, A., dumas, C., Michel, E., Parrenin, F., and Ritz, C.: Dome C migration in Antarctica during the last 800,000 years, ESS Open Archive, 2026, https://doi.org/10.22541/essoar.176833267.78739367/v1, 2026.

van Calcar, C. J., van de Wal, R. S. W., Blank, B., de Boer, B., and van der Wal, W.: Simulation of a fully coupled 3D glacial isostatic adjustment – ice sheet model for the Antarctic ice sheet over a glacial cycle, Geoscientific Model Development, 16, 5473–5492, https://doi.org/10.5194/gmd-16-5473-2023, 2023.

van Calcar, C. J., Whitehouse, P. L., van de Wal, R. S. W., and van der Wal, W.: Approximating 3D bedrock deformation in an Antarctic ice-sheet model for projections, The Cryosphere, 20, 757–775, https://doi.org/10.5194/tc-20-757-2026, 2026.

Van Liefferinge, B. and Pattyn, F.: Using ice-flow models to evaluate potential sites of million year-old ice in Antarctica, Climate of the Past, 9, 2335–2345, https://doi.org/10.5194/cp-9-2335-2013, 2013.

Van Liefferinge, B., Pattyn, F., Cavitte, M. G. P., Karlsson, N. B., Young, D. A., Sutter, J., and Eisen, O.: Promising Oldest Ice sites in East Antarctica based on thermodynamical modelling, The Cryosphere, 12, 2773–2787, https://doi.org/10.5194/tc-12-2773-2018, 2018.

van Wessem, J. M., Van De Berg, W. J., Noël, B. P., Van Meijgaard, E., Amory, C., Birnbaum, G., Jakobs, C. L., Krüger, K., Lenaerts, J. T., Lhermitte, S., et al.: Modelling the climate and surface mass balance of polar ice sheets using RACMO2–Part 2: Antarctica (1979–2016), The Cryosphere, 12, 1479–1498, https://doi.org/10.5194/tc-12-1479-2018, 2018.

Vittuari, L., Zanutta, A., Gandolfi, S., Martelli, L., Ritz, C., Urbini, S., and Frezzotti, M.: Decadal migration of Dome C inferred by global navigation satellite system measurements, Journal of Glaciology, 71, e117, https://doi.org/10.1017/jog.2025.28, 2025.

Von Storch, H. and Zwiers, F. W.: Statistical analysis in climate research, Cambridge university press, 2002.

Wang, H., Tang, X., Xiao, E., Luo, K., Dong, S., and Sun, B.: Basal Melt Patterns around the Deep Ice Core Drilling Site in the Dome A Region from Ice-Penetrating Radar Measurements, Remote Sensing, 15, https://doi.org/10.3390/rs15071726, 2023a.

Wang, Z., Chung, A., Steinhage, D., Parrenin, F., Freitag, J., and Eisen, O.: Mapping age and basal conditions of ice in the Dome Fuji region, Antarctica, by combining radar internal layer stratigraphy and flow modeling, The Cryosphere, 17, 4297–4314, https://doi.org/10.5194/tc-17-4297-2023, 2023b.

Weertman, J.: On the Sliding of Glaciers, Journal of Glaciology, 3, 33–38, https://doi.org/10.3189/S0022143000024709, 1957.

Westhoff, J., Ardoin, L., Weikusat, I., Blard, P. H., Fripiat, F., Seth, B., Soussaintjean, L., Krebs, M., Bouchet, M., Chung, A., et al.: 316 m of ice beyond the stratified sections of the Beyond EPICA Little Dome C ice core, https://doi.org/10.21203/rs.3.rs-9883712/v1, 2026.

Winkelmann, R., Martin, M. A., Haseloff, M., Albrecht, T., Bueler, E., Khroulev, C., and Levermann, A.: The Potsdam Parallel Ice Sheet Model (PISM-PIK) – Part 1: Model description, The Cryosphere, 5, 715–726, https://doi.org/10.5194/tc-5-715-2011, 2011.

Winter, A., Steinhage, D., Creyts, T. T., Kleiner, T., and Eisen, O.: Age stratigraphy in the East Antarctic Ice Sheet inferred from radio-echo sounding horizons, Earth System Science Data, 11, 1069–1081, https://doi.org/10.5194/essd-11-1069-2019, 2019.

Wirths, C., Hermant, A., Stepanek, C., Stocker, T. F., and Sutter, J. C.: Sequence of abrupt transitions in Antarctic drainage basins before and during the Mid-Pleistocene Transition, Nature Communications, 16, 10 391, https://doi.org/10.1038/s41467-025-65375-x, 2025.

Wirths, C., Yun, K.-S., Timmermann, A., Fischer, H., Stocker, T. F., and Sutter, J. C. R.: Estimating the impact of ice sheet surface height and ice divide variability on ice core based climate reconstructions, EGUsphere, 2026, 1–30, https://doi.org/10.5194/egusphere-2026-4275, 2026.

Wolovick, M. J., Moore, J. C., and Zhao, L.: Joint Inversion for Surface Accumulation Rate and Geothermal Heat Flow From Ice-Penetrating Radar Observations at Dome A, East Antarctica. Part II: Ice Sheet State and Geophysical Analysis, Journal of Geophysical Research: Earth Surface, 126, e2020JF005 936, https://doi.org/10.1029/2020JF005936, e2020JF005936 2020JF005936, 2021a.

Wolovick, M. J., Moore, J. C., and Zhao, L.: Joint Inversion for Surface Accumulation Rate and Geothermal Heat Flow From Ice-Penetrating Radar Observations at Dome A, East Antarctica. Part I: Model Description, Data Constraints, and Inversion Results, Journal of Geophysical Research: Earth Surface, 126, e2020JF005 937, https://doi.org/https://doi.org/10.1029/2020JF005937, e2020JF005937 2020JF005937, 2021b.

Xiao, C., Li, Y., Hou, S., Allison, I., Bian, L., and Ren, J.: Preliminary evidence indicating Dome A (Antarctica) satisfying preconditions for drilling the oldest ice core, Chinese Science Bulletin, 53, 102–106, https://doi.org/10.1007/s11434-007-0520-6, 2008.

Zhao, L., Moore, J. C., Sun, B., Tang, X., and Guo, X.: Where is the 1-million-year-old ice at Dome A?, The Cryosphere, 12, 1651–1663, https://doi.org/10.5194/tc-12-1651-2018, 2018.